Fermilab
Electron Cooling Experiment

Design Report

August, 1978

Fermi National Accelerator Laboratory
Batavia, Illinois

Operated by Universities Research Association Inc.
Under Contract with the United States Department of Energy

INDEX

Section	
I.	Introduction
II.	Electron Cooling
III.	Electron Cooling Region
IV.	Cooling-Ring Lattice Design
V.	Magnet System
VI.	Cooling-Ring Vacuum System
VII.	Injection and Accumulation
VIII.	RF System
IX.	Radiation Safety
X.	Instrumentation
XI.	Controls
	Appendix I
	Appendix II
XII.	Bibliography

Participants: J. Bridges, J. Gannon, E.R. Gray, J. Griffin, F.R. Huson, D.E. Johnson, W. Kells, F.E. Mills, C. Moore, G. Nicholls, L. Oleksiuk, T. Rhoades, D.E. Young, Fermilab; P.M. McIntyre, C. Rubbia, Harvard; W.B. Herrmannsfeldt, SLAC; D. Cline, J. Rhoades, Wisconsin.

DESIGN REPORT

FERMILAB ELECTRON COOLING EXPERIMENT

I. Introduction

The "cooling" of protons by electrons has been studied by the accelerator group of the Institute of Nuclear Physics at Novosibirsk. They have achieved damping of proton-betatron oscillations by Coulomb interaction with "cold" electrons as described by simple theory. They also observe fast damping when the longitudinal velocities of all the protons and electrons are very nearly the same and the electrons are trapped in a longitudinal solenoidal magnetic field. This effect results from the extended interaction between the same electrons and protons.

The Fermilab Electron Cooling Project will endeavor to extend the results of the Novosibirsk group by constructing a 200-MeV storage ring to cool and accumulate protons (and, in the future, antiprotons) at a rate of 15 Hertz.

The primary goal of this experiment will be to achieve the cooling and accumulation of protons, but, where possible, everything will be made compatible with cooling at 15 Hertz and accumulation of more than 10^{10} antiprotons in 3 hours. The acceptance of the storage ring will match that of the booster, because the booster is in the chain of accelerators necessary to accumulate and accelerate antiprotons. The design of the cooling ring and experiment are discussed in the body of this report. In Sections II and III, we discuss electron cooling, in Section IV the lattice, in V the magnets, in VI the vacuum system, in VII injection and accumulation, in VIII the RF section, in IX radiation safety, in X instrumentation, and in XI the controls.

II. Electron Cooling

The electron cooling process corresponds to the thermal relaxation of two fully ionized plasmas (protons and electrons) having different initial temperatures (see Fig. 1). To the extent that $\langle v_e \rangle \sim \langle v_p \rangle$, the protons will transfer thermal motion to the electrons, and approach an equipartition of energy $T_p = T_e$. The relaxation mechanism is parallel

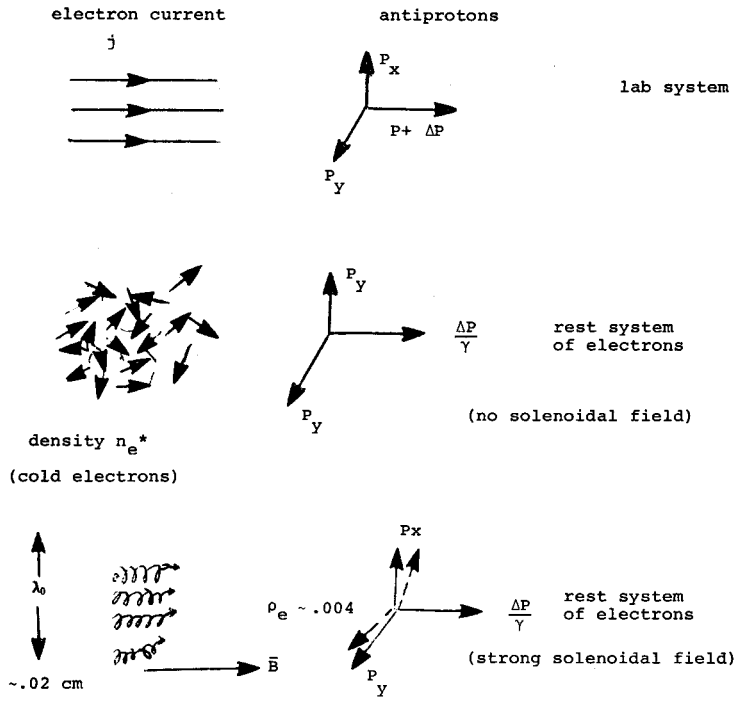

Fig. 3 Cooling Antiprotons by Electrons, first established by G.I. Budker et. al.

momentum transfer via the Debye-shielded Coulomb interaction in a strong solenoidal magnetic field.

The initial temperature of the protons is obtained from the beam emittance ε_H, ε_V and momentum spread $\Delta p/p$, and the lattice parameters β_H, β_V, X_p. For our cooling ring design,

$$\theta_H = \sqrt{\varepsilon_H/\pi\beta_H} = \pm\ 1.2 \text{ mrad} \quad a_H \sqrt{(\sqrt{\varepsilon_H\beta_H/\pi})^2 + (X_p\Delta p/p)^2} = \pm 2.2 \text{ cm}$$

$$\theta_V = \sqrt{\varepsilon_V/\pi\beta_V} = \pm\ 0.9 \text{ mrad} \quad a_V = \sqrt{\varepsilon_V\beta_V/\pi} = \pm\ 1.9 \text{ cm}$$

$$\Delta p/p = \pm 1.5 \times 10^{-3}$$

We can define a longitudinal and a transverse temperature:

$$T_\parallel = m_p \langle v_\parallel^{*2}\rangle = m_p c^2\beta^2 \quad (\Delta p/p)^2 = 670 \text{ eV}$$

$$T_\perp = m_p \langle v_\perp^{*2}\rangle = m_p c^2\beta^2\gamma^2\langle\theta_H^2+\theta_V^2\rangle = 988 \text{ eV}$$

Thus, initially the proton temperature is

$$T_p = T_\parallel + T_\perp = 1658 \text{ eV}$$

The condition $v_e^* \sim v_p^*$ for optimal initial cooling corresponds to

$$T_e \sim T_p\ (m_e/m_p) = .82 \text{ eV}.$$

We will evaluate some of the plasma properties of the electrons and protons which are relevant to the cooling process. The parameters j_e = 1.5 A/cm^2, β = .57, γ = 1.21, B = 1 kG, T_e = .5 eV, ℓ = 5 m of the actual electron beam are used in all calculations.

<u>Debye length</u>: $\lambda_D = \sqrt{T/4\pi e^2 n_e^*} = .051 \sqrt{\beta\gamma T/j_e} = .025$ cm.

This is the screening length for space charge cancellation of long-range Coulomb interactions.

<u>Plasma parameter</u>: $N_D = (4\pi\lambda_D n_e^*/3)^{-1} = 1.2 \times 10^5 \sqrt{T^3\beta\gamma/j}$

$$= 2.9 \times 10^4$$

This is the number of electrons in a Debye sphere, and represents the statistical quality of the plasma.

<u>Plasma frequency</u>: $\omega_e = \sqrt{4\pi n_e^{*2}/m_e} = 8.1 \times 10^8 \sqrt{j_e/\beta\gamma}$

$$= 1.2 \times 10^9 \text{ rad/sec.}$$

This is the characteristic ring frequency with which the plasma responds to fluctuations.

<u>Cyclotron Frequency</u>: $\Omega_e = eB/m_e c = 1.76 \times 10^7 B$

$$= 1.76 \times 10^{10} \text{ rad/sec.}$$

$$\Omega_p = eB/m_p c = 9.6 \times 10^3 B$$
$$= 9.6 \times 10^6 \text{ rad/sec}$$

<u>Gyroradius</u>: $\rho_e = v^*/\Omega_e = 2.38\sqrt{T_\perp}/B = 1.7 \times 10^{-3}$ cm.

Note that the gyroradius of an electron is an order of magnitude smaller than the Debye length. Thus, electrons are not free to move within a Debye sphere, and the mechanism of space charge shielding is more complicated than given in the standard treatments.

<u>Collision Freuqncy</u>: $\nu = n_e^* \langle \sigma v^* \rangle = \left(\frac{\pi}{2}\right)^{3/2} \frac{e^4 n^*}{m^{1/2} T^{3/2}} \log \Lambda$ where $\log \Lambda = \log(12\pi n_e^* \lambda_D^3) = 12.4$ is the Coulomb logarithm for free scattering in a Debye-shielded potential ($b_{max} = \lambda_D$)

$$\nu_e = 2.7 \times 10^4 \text{ sec}^{-1}.$$

Note that $\Omega_e/2\pi \simeq 10^5 \nu_e$. Thus, many gyrations take place between collisions. This coherence can be quite important to the cooling process. The collision time is also the relaxation time for the electron distribution, which therefore is not appreciably changed during the single traversal of the straight section.

We can now evaluate the effective temperature of the actual electron beam. There are several contributions:

1) A mismatch of the local magnetic field to the electrostatic trajectory of the electrons will cause them to begin spiraling about the field direction and increase the transverse temperature from the cathode temperature $T_K = 1050^\circ C = .1$ eV:

$$T_\perp = T_K + m_e r^2 \Omega_e^2 (\delta B/2B)^2 = .1 + 2.75 \times 10^5 \ (\delta B/B)^2.$$

We have designed a magnetic field configuration for which $\delta B/B \lesssim 10^{-3}$, so $T_\perp \sim .4$ eV.

2) There is a space charge depression across the electron beam profile of $\Delta V = \pi j_e r^2/\beta\gamma c$. In an unneutralized beam with $j_e = 1.5$ A/cm^2; $r = 2.5$ cm, this depression is 1200 V. It produces an effective longitudinal temperature:

$$\Delta T_\parallel \simeq \alpha^2 e^2 \Delta V^2/\beta^2\gamma^2 m_e c^2 = (\alpha e \Delta V/500)^2$$

where $\alpha < 1$ is the fraction of unneutralized electron current. By trap-

ping positive ions in the cooling region, it is possible to neutralize the beam to the limit $\alpha e\Delta V \to T \sim .5$ eV. The remaining effect is then regulation of the acceleration voltage, $\delta V \sim 5$ V. The limit is then $\Delta T \to 10^{-4}$ eV. For a cold neutralized electron beam, $T_{\parallel} << T_{\perp}$ and $T_e \sim T_{\perp} \simeq .4$ eV. For an unneutralized beam, $T_{\parallel} \sim 1$ eV.

It should be noted that full space charge neutralization may create plasma instabilities, particularly the two stream instability. The growth time and amplitude of resulting potential fluctuations will be investigated.

The temperature relaxation between protons and electrons can be expressed conveniently in terms of a friction force acting on the protons as a result of collisions. In the absence of magnetic field, we have

$$\vec{F}\,(\vec{v}_p,\vec{r}_p) = -\frac{4\pi e^4 n_e^*}{m_e}\,\log\Lambda \int \frac{(\vec{v}_p - \vec{v}_e)}{\left|\vec{v}_p - \vec{v}_e\right|^3} f_e(\vec{v}_e,\vec{r}_p)\,d^3\vec{v}_e \qquad (1)$$

This expression provides an intuitive <u>electrostatic analogy</u>. The integral in Eq. 1 is just the twin (in velocity space) of the Coulomb force of a charge distribution acting on a test charge.

The function $\vec{F}(\vec{v}_p,\vec{r})$ for a spherically symmetric electron velocity distribution $f_e(v_e)$ is shown in Fig. 2. For small proton velocity ($v_p << v_e$), F increases linearly with $\vec{v}_p$. For large proton velocity ($v_p >> v_e$), F decreases as $1/v_p^2$. To calculate the damping rate we note that

$$\vec{F}(v_p,r_p) = \frac{4\pi e^4 n_e^*}{m_e}\,\log\Lambda\,\vec{\nabla}_{v_p} I$$

where $I = \int \frac{f_e(\vec{v}_e)}{\left|\vec{v}_e - \vec{v}_p\right|} d^3\vec{v}_e$ is the Rosenbluth potential and is evaluated in the literature.

Thus, the damping rate for the six-dimensional phase space of the proton is:

$$\lambda_p^* = \frac{1}{m}\,\vec{\nabla}_{v_p} \cdot \vec{F} = \frac{4\pi e^4 n_e^*}{m_e m_p}\,\log\Lambda\,\nabla^2_{v_p} I = \frac{(4\pi)^2 e^4 n_e^*}{m_e m_p}\,\log\Lambda\, f_e\,(\vec{v}_p)\,.$$

where $f_e(\vec{v}_p)$ is just the electron velocity distribution function evalua-

$$\vec{F} = -\frac{4\pi\, e^4\, n_e^*}{m_e} \log\left(\frac{b_{max}}{b_{min}}\right) \vec{\nabla} \int \frac{f(\vec{v}_e)\, d^3\vec{v}_e}{\left|\vec{v}_p - \vec{v}_e\right|}$$

$$\lambda = \vec{\nabla}\cdot\vec{F}/m_p = \frac{4\pi\, e^4 n_e^*}{m_e\, m_p} \log\left(\frac{b_{max}}{b_{min}}\right) f(\vec{v}_p)$$

$$\lambda \propto T_e^{-3/2}$$

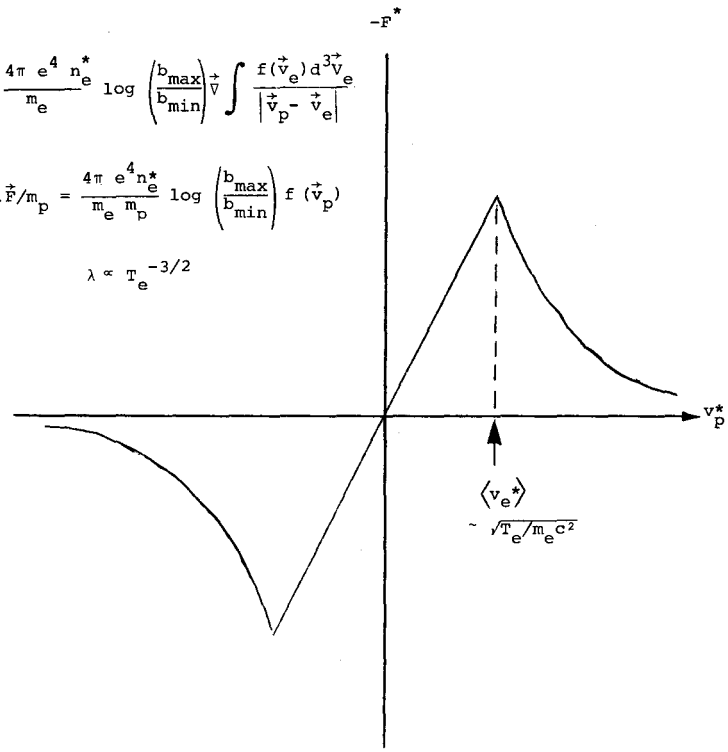

Fig. 2 Friction Force vs. Proton Velocity in Rest Frame

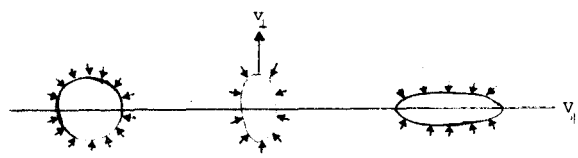

ted at v_p. If the velocity distribution is not symmetric, we can use the electrostatic analogy to understand what happens. On a surface of uniform density in velocity space, F is directed everywhere into the surface (see Fig. 2). If $\langle v_{e_\parallel}^2\rangle \gg \langle v_{e_\perp}^2\rangle$, the velocity distribution is cigar shaped, and the friction force acts in the transverse plane. If $\langle v_{e_\parallel}^2\rangle \ll \langle v_{e_\perp}^2\rangle$, the velocity distribution is disc-shaped, and the friction force acts in the longitudinal direction.

In general, $$f_e(\vec{v}_p) = \frac{\exp\{-m_e v_\parallel^2/2T_\parallel - m_e v_\perp^2/2T_\perp\}}{(2\pi)^{3/2}(T_\perp/m_e)(T_\parallel/m_e)^{1/2}}$$

and $$\lambda^* = \frac{4\sqrt{2\pi}\, r_e r_p n_e^* c \log\Lambda}{(T_\perp/m_e c^2)(T_\parallel/m_e c^2)^{1/2}} \exp(-m_e v_\parallel^2/2T_\parallel - m_e v_\perp^2/2T_\perp)$$

We can now evaluate the damping rate for the parameters of the cooling region. The damping rate in the laboratory is obtained by the transformation

$$t = \gamma t^*, \quad n_e = \gamma n_e^* = j_e/e\beta c$$

For protons with $v_p < v_e$, the exponential in Eq. 2 is ~1, so

$$\lambda = \frac{4\sqrt{2\pi}\, r_e r_p (j_e/e) \log\Lambda}{\beta\gamma^2 (T_\perp/m_e c^2)(T_\parallel/m_e c^2)^{1/2}}\eta = 62\eta = 3.1/\text{sec}$$

where $\eta = .05$ is the fraction of the ring circumference in which electron cooling takes place.

The above analysis of electron cooling neglects any effects arising from the strong solenoidal magnetic field. The importance of the magnetic interaction is demonstrated by the fact that $\rho_e \ll \lambda_D$, so that electrons are individually trapped on a scale small with respect to the shielding length. It is convenient to analyze collisions separately in three regions of impact parameter:

1) $b < b_o$, where the impulse received by the electron is comparable to or greater than the mean $v_e \gamma b_o = r_e c^2/\langle v_e^2\rangle \sim 10^{-7}$ cm;

2) $b_o < b < \rho_e$; and

3) $\rho_e < b < \lambda_D$.

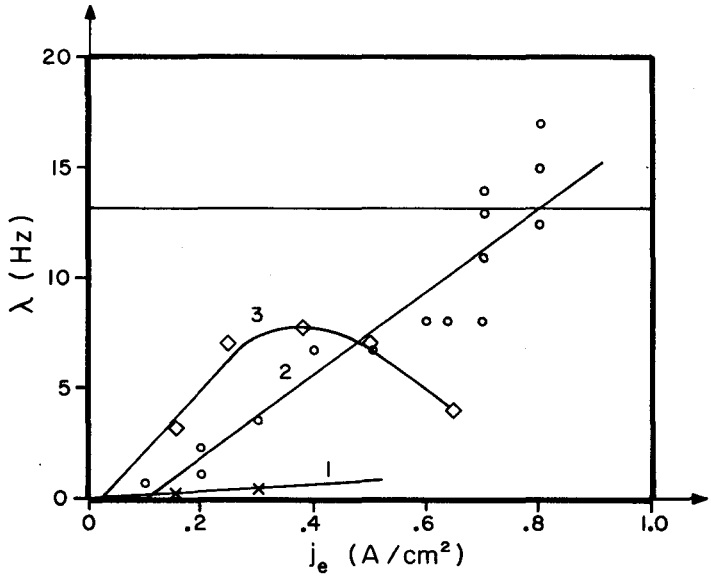

Fig. 3 Cooling Rate Lambda as a Function of Electron Current Density J_e for Three Electron Gun Geometries, from recent Novosibirsk results.

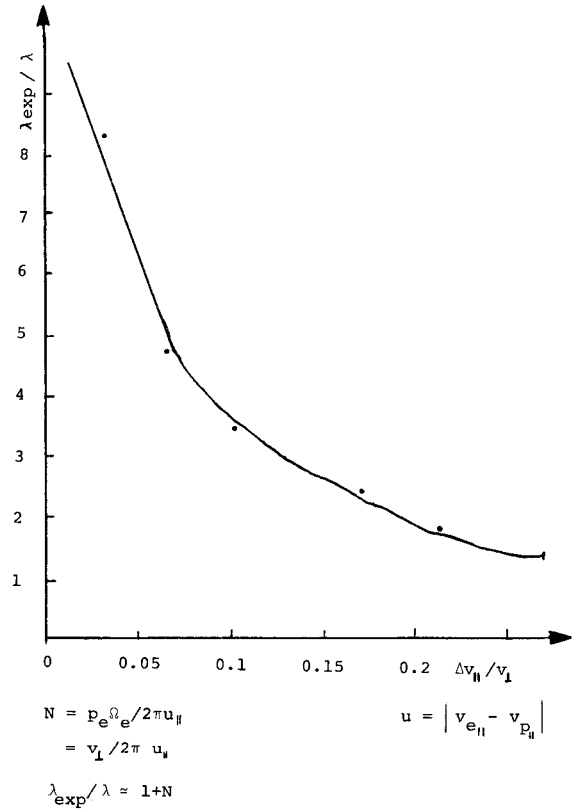

Fig. 4 Coherent Cooling for $V_{\parallel} << V_{\perp}$

In region 2, the electron scatters with impact parameter b repeatedly as it spirals about its field lines. The transverse component of the impulse in each collision acts to adiabatically twist the axis of spiral motion, but leaves the impact parameter roughly constant. In region 3, the electron is in effect constrained to move on a line, and the proton scatters coherently from it over a relatively long time.

The coherence of the friction force in regions 2 and 3 can be visualized most simply in the approximation that the Coulomb interaction of a given electron with a proton has the same transverse closest-distance-of-approach on successive orbits of its spiral motion. The electron cooling is then enhanced by a factor which is just the number of spirals which occur while the electron is still within a distance ρ_e of the proton, due to its longitudinal velocity. Thus

$$1/\tau = (1/\tau_o)(1+\rho_e\Omega_e/2\pi\langle v_{\parallel}\rangle) = (1/\tau_o)(1+\langle v_{\perp}\rangle/2\pi\langle v_{\parallel}\rangle).$$

When $\langle v_{\parallel}\rangle \ll \langle v_{\perp}\rangle$, this coherence dominates the cooling process.

The results of Budker et al. for electron cooling of 80 MeV protons are shown in Figs. 3 and 4. Figure 3 shows the dependence of cooling rate on electron beam current for several electron gun geometries. The slope for each geometry is different, corresponding to different effective electron temperatures T_e. The effect of space charge is clearly shown in curve 3, where the cooling rate is limited for high current by the increasing space charge depression.

Figure 4 shows the effect of varying $\langle v_{\parallel}\rangle / \langle v_{\perp}\rangle$ on cooling rate. The dependence is clearly well described by the simple coherence model discussed above.

III. Electron Cooling Region

The electron cooling of the stored proton beam occurs in the straight section shown in Figs. 5,6. The design must provide a cold, intense electron beam and bring it into near perfect alignment with the proton beam. The electrons are confined in the drift region by a 1 kG solenoidal magnetic field to avoid divergence produced by space charge forces.

Electron Gun

The electron beam must have a rest frame temperature $T_e \leq 1$ eV (see Section II). To produce such a low temperature, the electron gun has been designed with a classic Pierce geometry, and is itself immersed in the magnetic field. This means that the field lines threading through the cathode follow the trajectories and ultimately all the way through the collector. Otherwise, the electrons would gyrate around the actual magnetic field direction, and increase greatly the transverse temperature. We have chosen to use the electron gun design developed for the SPEAR klystron. It produces a 28A, 27 cm^2 beam at 110 kV. The dispenser cathode can be reactivated repeatedly after exposure to air. Figure 7a shows the field design of the gun and the calculated electron trajectories. The defocusing lens action of the anode causes the electrons to spiral, resulting in the undulation clearly visible in Fig. 7a. This undulation can be cancelled by a "resonant" focusing system, as shown in Fig. 7b. Electrode potentials are adjusted to match the spiral motion so that the electrons immerge parallel. Improper field matching causes the same effect as shown in Fig. 7a with no focusing system.

Drift Region

After leaving the gun, the beam is bent 90° to superimpose it on the proton beam. The bending is accomplished with a crossed toroidal and dipole magnetic field. The resulting trajectory bends through a circular arc without exciting gyrations. The toroid has a gradient of 6.7 kG/m, and a dipole field of 80 G.

The cooling takes place in a 5 m long drift region, where the electron beam is confined by a uniform-field solenoid. We have chosen a solenoidal field $B_o = 1$ kG as being adequate both for beam confinement and

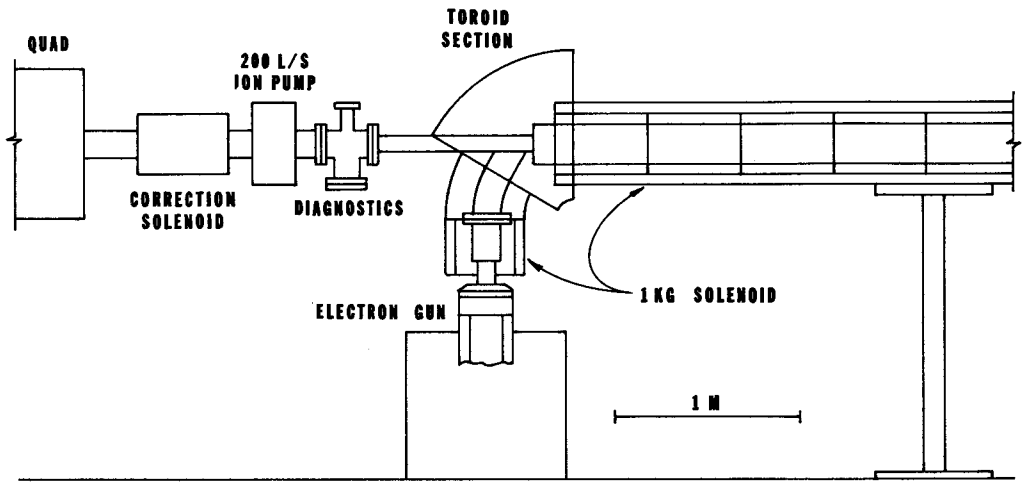

Fig. 5 Electron Cooling Straight Section

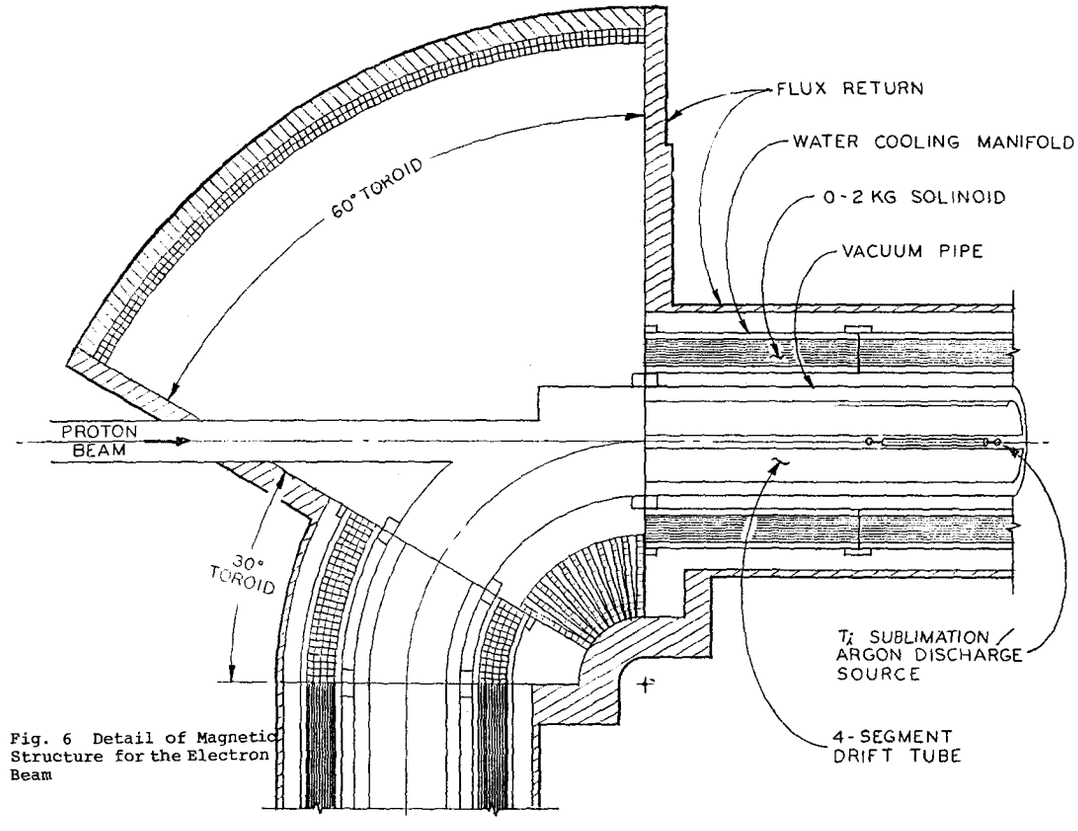

Fig. 6 Detail of Magnetic Structure for the Electron Beam

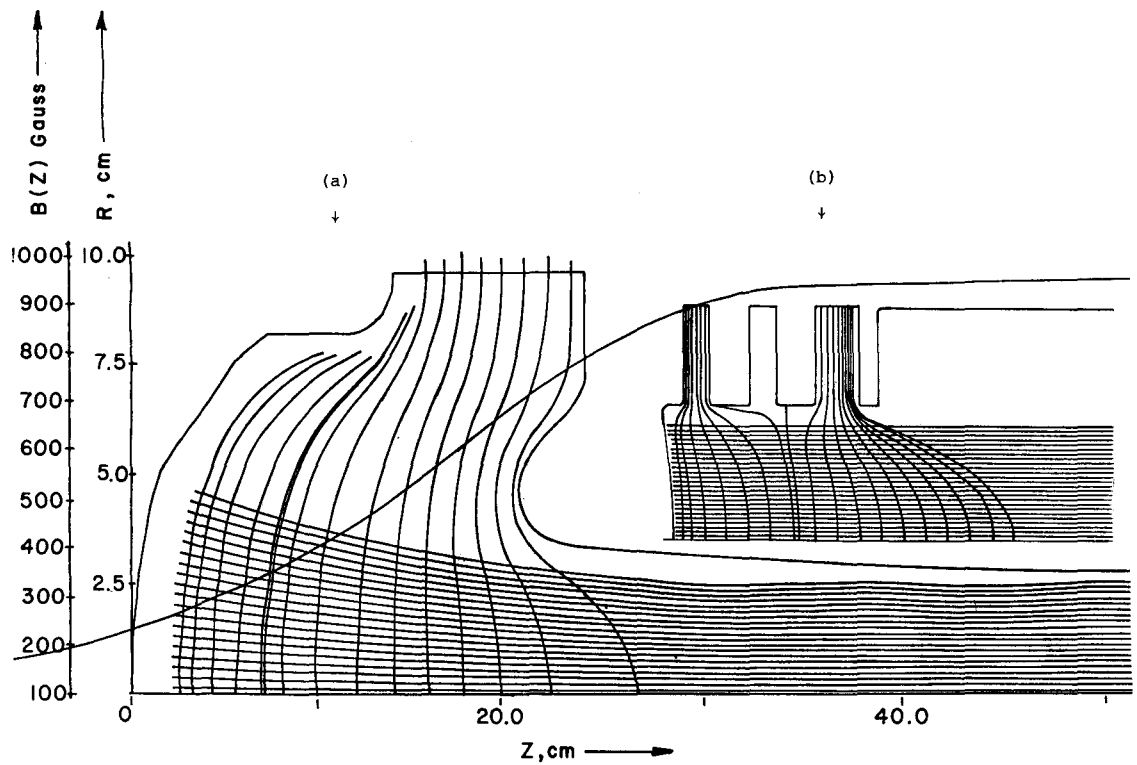

Fig. 7 Electron Beam Trajectories in the Gun Region. Also shown is the Axial Magnetic Field b.

for studying coherent cooling phenomena. The solenoid is an assembly of 0.5 m long coils of anodized aluminum strip conductor. The field produced by a long sequence of the coils with minimum spacing has a uniformity $(\delta B/B)_{rms} \leq 5 \times 10^{-4}$, sufficient for optimal electron cooling.

The ground potential surface throughout the bending and cooling region is a drift tube of 6' diameter. This drift tube is split longitudinally into four segments, and each segment is connected to an independent voltage source (see Fig. 6). In this way, we can control the "ground" potential, and introduce dipole and/or quadrupole electric fields if desired.

By depressing the "ground" in the cooling region several kV below the ground in the short drift sections in each 60° bend, it is possible to trap the ions formed by beam gas scattering in the cooling regions, and neutralize the space charge in the electron beam (see Section IV). The ion density needed has a pressure of equivalent of

$$P_i = \frac{1.6 \times 10^{-8}}{Z} \text{ Torr.}$$

Since the beam growth is proportional to $P_i Z_i^2$, it is desirable to use hydrogen for neutralization.

Depressed Collector

After a second 90° bend, the beam is decelerated and absorbed in a collector assembly. In order to minimize the power dissipation (full beam power is 2.6 MW), the collector is operated at a potential only slightly ($\delta E \sim$ few kV) lower than that of the electron gun cathode. The collection is then efficient only if no electrons have lost more than δE of energy since their birth at the gun cathode. Any energy coupled to gyration in the deceleration process is difficult to recover into longitudinal motion. For this reason, the collector geometry closely approximates that of the gun itself, including the carefully tapered magnetic field. Figure 8 shows the field optics and equipotentials in the collector region.

One difficulty in maximizing the collection efficiency at the collector is secondary emission from the collector surface. Figure 9 shows

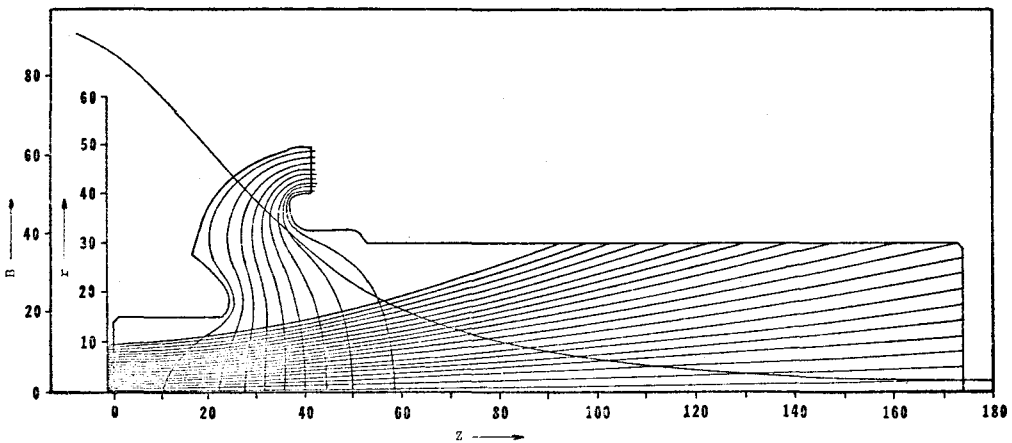

Fig.8 Electron Beam Trajectories in the Collector; potential depression 2 kV. Also shown is the axial magnetic field strength B.

the secondary emission backscatter yield on various materials; the spectrum of backscattered electrons is shown in Fig. 10.[1] About 7% of primary electrons produce a secondary electron having energy near that of the primary . These electrons are roughly isotropic, and only a fraction $\lesssim 10\%$ enter the effective acceptance of the accelerating column.

The space charge on the inner rays of the beam causes most secondary electrons to be re-accelerated into the surface. Only secondaries from the outer rim of the beam can escape without space charge suppression. The resulting re-circulating beam should constitute a fraction $\sim 10^{-4} - 10^{-3}$ of the primary beam when collector potentials are optimized.

A second way of reducing secondary emission effects is to coat the copper collector surface with a film of material having low secondary emission coefficient such as titanium or platinum. This technique will be employed should remanent secondary emission create problems.

Vacuum

The extreme tolerance on magnetic field uniformity precludes any gaps in the solenoid wide enough to accommodate pumping ports in the electron cooling region. To ensure an adequate vacuum ($<10^{-10}$ Torr), Ti sublimation pumps are located in the 1" gap between the drift tube and vacuum pipe wall at intervals along the cooling region (see Fig. 6). The sublimation units can also be used as electrodes for ion discharge cleaning of the entire cooling region. The segments of the drift tube can also be used as the electrodes of an omegatron, where the crossed magnetic field is that of the solenoid. This allows convenient analysis of the gas composition in the neutralizing ion cloud.

Beyond each of the 90° bends is located a 220 ℓ/sec triode ion pump, and an oil free rough vacuum system as shown in Fig. 5. Each ion pump has a potential screen to prevent the escape of fast ions which could penetrate the ion trap in the cooling region and damage the gun by ion bombardment.

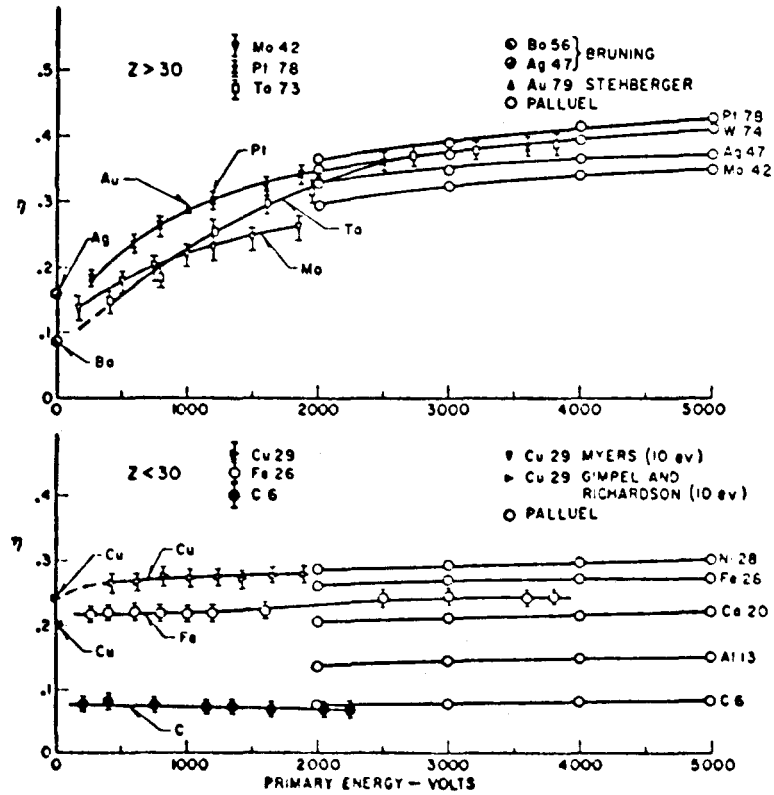

Fig. 9. Variation of backscattered fraction η with incident energy. Upper diagram—elements of Z>30. Lower diagram—elements of Z<30. Taken from, E.J. Sternglass, Phys. Rev. 95, 2, 345, (1954).

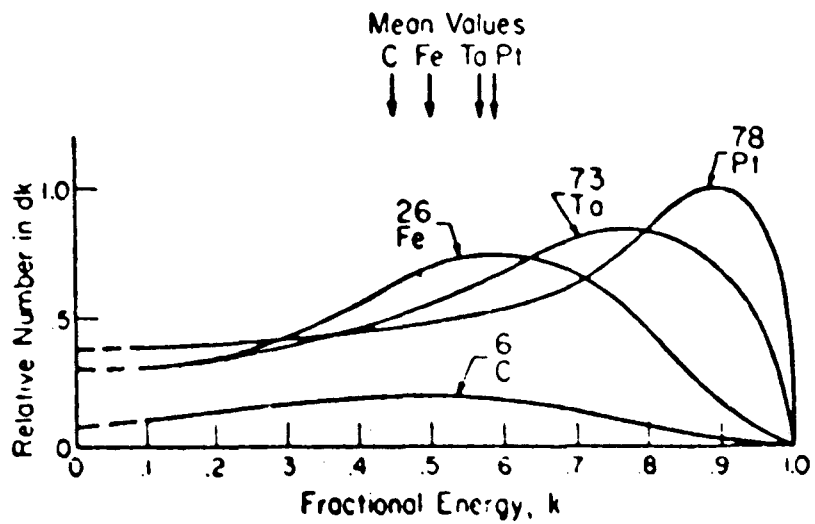

Fig. 10. Energy spectra of backscattered electrons for C, Fe, Ta, and Pt in energy range from 0.5-2 keV. Areas in ratio of total backscattered fraction η. Taken from, E.J. Sternglass, Phys. Rev. 95, 2, 345, (1954).

Correction Elements

The proton beam must be compensated for the small perturbation in traversing the toroidal and solenoidal fields in the electron cooling region. The solenoidal field causes a gyration of each proton by $\delta = \Omega_p \ell/c = 40$ mrad/revolution. This betatron skew coupling will be compensated by two skew quadrupoles, located on each end of the long straight section.

The proton beam also experiences a tune shift due to the focusing effect of the electron beam. This effect has been incorporated into the lattice design, decoupling the quadrupoles flanking the cooling straight section from their mates on the opposite side of the ring. The tune can be easily corrected throughout the operating range of electron beam current.

The proton beam experiences a vertical dipole field $B\ell \sim .1$Tm in the toroids. The beam alignment is corrected by small dipoles just beyond each end of the cooling region.

Electron Beam Diagnostics

As there are no standard diagnostic tools available to probe an intense electron beam non-destructively and measure its temperature and space charge depression. We are developing 3 new techniques for measuring these parameters in the cooling straight section.

A. Secondary Electron Beam

We have a small electron gun of energy 8.7 keV current 0.2 A, beam diameter 0.08 cm. This tiny gun is useful for several diagnostics:

Magnetic Field Alignment and Correction It is necessary to align the magnetic field in the solenoid to an accuracy of ~0.2 mrad with respect to the proton beam. The field must be corrected to achieve the desired adiabatic electron trajectories in the toroidal regions at each end. These tasks can most easily be performed using the small electron beam in the absence of the main e-beam. Its maximum gyroradius is $\rho_{max} < 2.38\ \sqrt{T_e}/B = 0.2$ cm even when the full 8.7 keV energy is transformed into gyromotion. A phosphor screen placed to intercept the beam at a var-

iable depth allows us to trace the magnetic lines of force though the entire electron beam with a transverse resolution of ~0.02 cm.

Space Charge Depression Suppose the small electron gun is now aligned parallel to the main beam, but displaced radially to be outside the main beam at a radius r. The equation of motion for an electron in the small beam is then

$$\dot{\vec{v}} + (\vec{v} \cdot \vec{\nabla})\, \vec{v} = \frac{e}{m}\, (\vec{E} + \vec{v} \times \vec{B})$$

The radial component is $\dot{v}_r - \frac{v_\theta^2}{r} = \frac{e}{m}\,(E_r + v_\theta B)$. The electric field outside the main e-beam, with neutralized fraction α, is

$$E_r = -\alpha\, \frac{n_e e R^3}{2\varepsilon_o r^2} = \frac{\omega_e^2}{2}\, \frac{R^3}{r^3}\,.$$

Requiring radial stability ($\dot{v}_r = 0$) yields the rotation frequencies $\omega = v_o/r$ of the small electron beam:

$$\omega^2 + \frac{\omega_e^2 \alpha R^3}{2r^3} - \omega\Omega_e = 0\ ;$$

$$\omega = \frac{\Omega_e \pm \sqrt{\Omega_e^2 - 2\omega_e^2\, \alpha\, R^3/r^3}}{2} \simeq \begin{cases} \Omega_e & \text{normal cyclotron motion} \\ \dfrac{\alpha\omega_e^2 R^3}{2\Omega_e r^3} & \text{slow spiral around primary beam} \end{cases}$$

The slow spiral motion has a frequency $\omega_s = \frac{\alpha\omega_e^2 R^3}{2\Omega_e r^3} = 5 \times 10^6\ \alpha$, rad sec^{-1} for radius r = 2R. This corresponds to a transverse displacement of $\delta = \omega_s rL/\beta C = 0.8\alpha$ cm during the length of the long solenoid. Thus we can easily measure the neutralized fraction α residual gas. The self-magnetic field of the main electron beam, which has been neglected here, makes a small calculable correction to the precession rate.

B. Laser Probe

A Compton backscatter device has been designed and is being assembled. Figure 11 illustrates the layout of this system. Infrared light

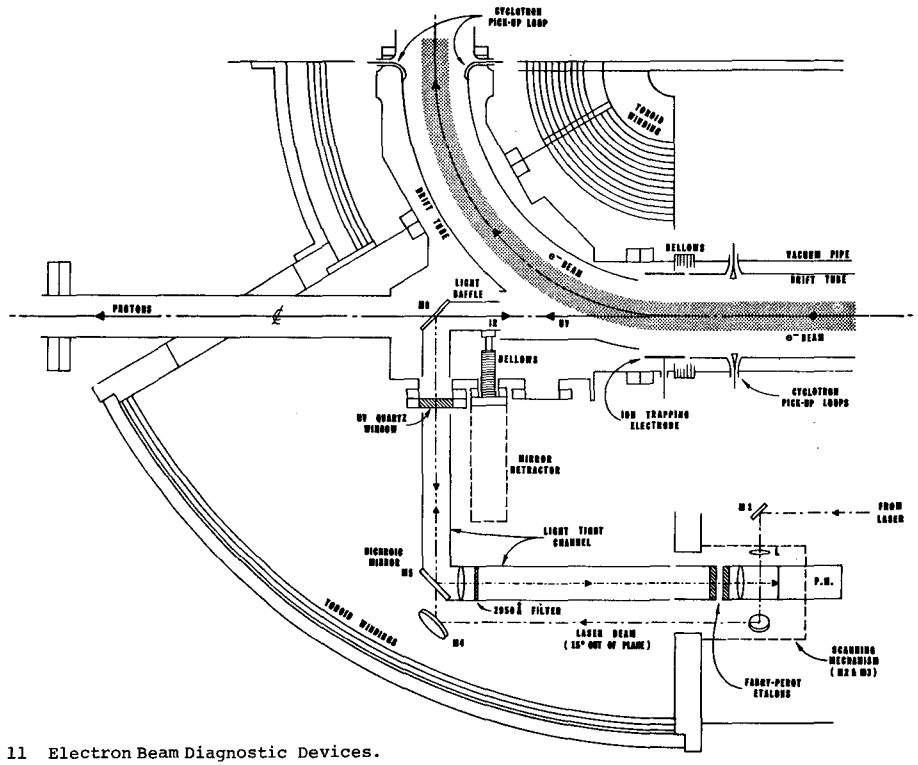

Fig. 11 Electron Beam Diagnostic Devices.

(1.06 μ) from a commercial laser with beam waist $\lesssim$1mm ϕ and $\leq$1mrad divergence is focused (L) into the oncoming electron beam. A mirror assembly remotely scans the laser beam both horizontally and vertically across the electron beam cross section. A final metal mirror (M6) injects the laser beam parallel to the electron beam inside the vacuum. This mirror is retractable via a bellows actuator from the (anti) proton orbits.

Compton backscatter is collected by part of the same optical pathway which the entering laser beam followed (M6-M5). Since the backscatter radiation is at 2900Å in the ultraviolet a bichroic beamsplitter may be used to separate it from the superimposed, entering IR light.

A detailed analysis of the performance of this system is described in Fermilab TM-771. Through the backscatter frequency dependence (p/ω) $d\omega/dp = 1.14$ ($p = e^-$ momentum) we can measure the longitudinal velocity profile of the electron beam. For instance, the full un-neutralized 30A beam will have a ~1300 V radial space charge depression which will produce a difference in backscatter wavelength of ~20Å from beam center to edge.

The backscattered light will be analyzed by a Fabry-Perot interferometer with free spectral range ≈20Å and resolution ≈1/2Å. A high quality PM (RCA C31000 M2C) with a uv window detects the signal. The solid angle of uv light collection is matched to the goal of 1/2Å overall resolution. The amount of light collection within this solid angle for full laser power (14 watts cw) and full electron current (30A) is 32 γ/s. Optimistically the detection system will be ~10% efficient. Since the laser can be pulsed we can obtain effective background rates <<1/sec.

The entire system (laser beam scanning, Fabry-Perot tuning and scanning, and signal collection) is remotely operable at the control console via the computer - CAMAC system.

C. Cyclotron Radiation Pick-up

Our ~1 kG axial containment field sets a ~3 GHz cyclotron frequency for the electrons. Thus transverse temperature may be measured by detecting microwave cyclotron radiation.

Although the monochromatic cyclotron frequency will be smeared considerably by Doppler shift to the Lab frame (for "free" electrons), electrons traveling down a tube (wave guide) will excite each accessible mode at only two discrete frequencies. A specific detector based on this principle (Fermilab TM-798) will be employed by us to monitor transverse temperature (Fig. 11).

Three pick-ups are employed, each consisting of a pair of diametrically opposed loops. Each toroid bend drift tube will have a pair. In these regions it will be desirable to detect the large coherent oscillations associated with the gun/collector "tuning". The straight section pick-up must be sensitive to residual totally incoherent cyclotron motion. For instance, the ~1000°C cathode will generate electrons with thermal energy of ~0.5 eV which will produce a pick-up signal of $\sim 10^{-11}$ watt (30A beam current) in ~20 MHz wide peaks. The associated noise using a 2 db noise figure preamplifier is 6×10^{-14} watt. However, there will be probably more troublesome smooth background due to the shot noise induced on the pick-up electrodes by the intense passing electron beam. This pedestal may be several times larger than the signal peak itself but should be easily accommodated by the dynamic range of our microwave spectrum analyzer.

D. Pin-ball Machine

We have designed a small magnetic induction cannon to fire a tiny stainless steel ball (r_o = 1 mm) through the beam with a velocity $v_o \sim 10$ m/sec (see Fig. 12). The total charge energy intercepted by the ball are

$$Q = j_e \pi r_o^2 R/v = 1.2 \times 10^{-4} C$$

$$E = Q \cdot V = 13J$$

This would result in a temperature rise $T = 3E/C_v \rho 4\pi r_o^3 = 870^oC$, well below melting point. The intercepted current is $i - I(r_o/R)^2 = 40$ mA, well within the performance of the HV supply. The mean range of 110 kV electrons in steel is .004 cm, so all electrons stop in the surface layer on the ball. The passage time through the beam is $t = 2R/v_o = 5$ msec. Heat relaxation in the bulk of the ball is effective since $c_s t = 5$ mm $\ll r_o$

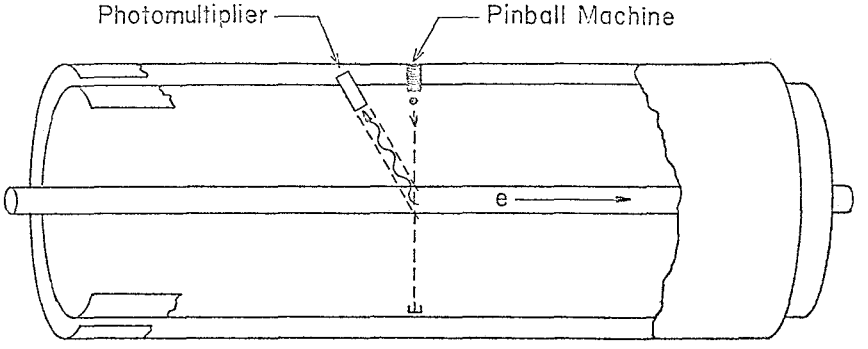

Fig. 12 Pinball Machine - e beam profile measurement

where $c_s \sim 1m/sec$ is the temperature relaxation in steel.

By looking at the scintillation light from the ball as a function of time, we can plot the density profile across the electron beam. A major uncertainty in this method is that the ball will charge up in a rather complicated way as it transverses the beam. On the other hand, the ball absorbs charge from the beam. But each incident electron has a backscatter coefficient of ~0.3. Also, as the ball charges up, electrons tend to bubble around it rather than collide; thus, the net response may be a function of position in the beam.

References

1. E.J. Sternglass, Phy. Rev. 95, 345 (1974).

IV Cooling Ring Lattice Designs

The main requirements on the design of a lattice structure in which to study electron cooling have already been given - (a) it should operate at 200 MeV; (b) the components must be reuseable as an antiproton lattice within the booster tunnel; (c) the extraction orbit should be a multiple of the booster wavelength; and (d) the long and short straight sections must have properties suitable for electron cooling and for injection. In addition, the usual requirements of operating in a region of the stability diagram far from resonances, not using more magnets or power supplies than necessary, etc., persist. Finally, there should be some flexibility to change the beam parameters in the cooling region to obtain the optimum cooling rates. The two requirements (b) and (c) above fix many of the variables for this lattice; in order to fit into the booster tunnel geometry, a structure must have at least 24 bend centers. Spacing between magnets and requirement (c) above, then fairly well fix the overall size of the lattice. The other requirements are all straightforwardly met and cause no major concern.

Three different structures are described below in varying detail. They consist of a design for an above-ground racetrack which has been optimized for electron cooling in a long straight section and injection into a shorter, straight section. A brief discussion of a possible design to fit within the present booster tunnel is given next, and finally a look is given into an expansion of the above ground racetrack into a booster length device.

A. Initial operation design

The requirement that the components of this lattice be able to be reassembled in the booster tunnel requires at least 24 bending dipoles with bend angle of 15° each. The most economical geometry using these dipoles is then to have two straight sections connected on each end with close-packed curved sections. The design chosen consists of two long straight sections in which the beam properties are adjusted to the desired values by means of matching quadrupoles connected to regular,

curved sections made of FODO cells. A short straight section, made by the omission of one bending magnet from a normal cell, has been put into the middle of each curved section to facilitate such devices as internal dump, beam monitors etc. at one end, and for injection at the other end. A general layout of this design is shown in Fig. 13. The beam size and momentum dispersion of the long and short straight sections have been chosen to be nearly optimal for electron cooling and multiple-turn injection (momentum stacking), respectively.

Two "initial design" lattices exist - one being simply a proton storage ring and the other compensating for the large tune shifts due to the focusing effect of a totally unneutralized electron beam of some 26 amps.[1,2] This linear compensation has been accomplished by retuning the three quadrupoles on either side of the electron beam. Any amount of possible vertical-horizontal coupling caused by the solenoid could be overcome through the use to two orghogonal, skew-quadrupoles as illustrated in Ref. 3, and the remaining perturbations on the proton beam due to the cooling section are to be locally corrected.

The lattice functions for one-half of these racetrack designs are plotted in Figs. 14 and 15 and their lattice properties listed in Table I. These plots correspond to the on-momentum beam. Because the closed orbits for the injected and stacked beams are not centered, the corresponding plots differ slightly from the ones shown. Note that Fig. 14 shows either half of the lattice without the electron beam while Fig. 15 shows the cooling half with the electron beam turned on. In this case, Fig. 14 is the other half of the design. Beam envelopes for horizontal and vertical planes for the case with the electron beam are shown in Figs. 16 and 17.

For the horizontal plane, both the initially injected beam and the rf displaced stacked beam are shown together with some separation for a septum thickness.

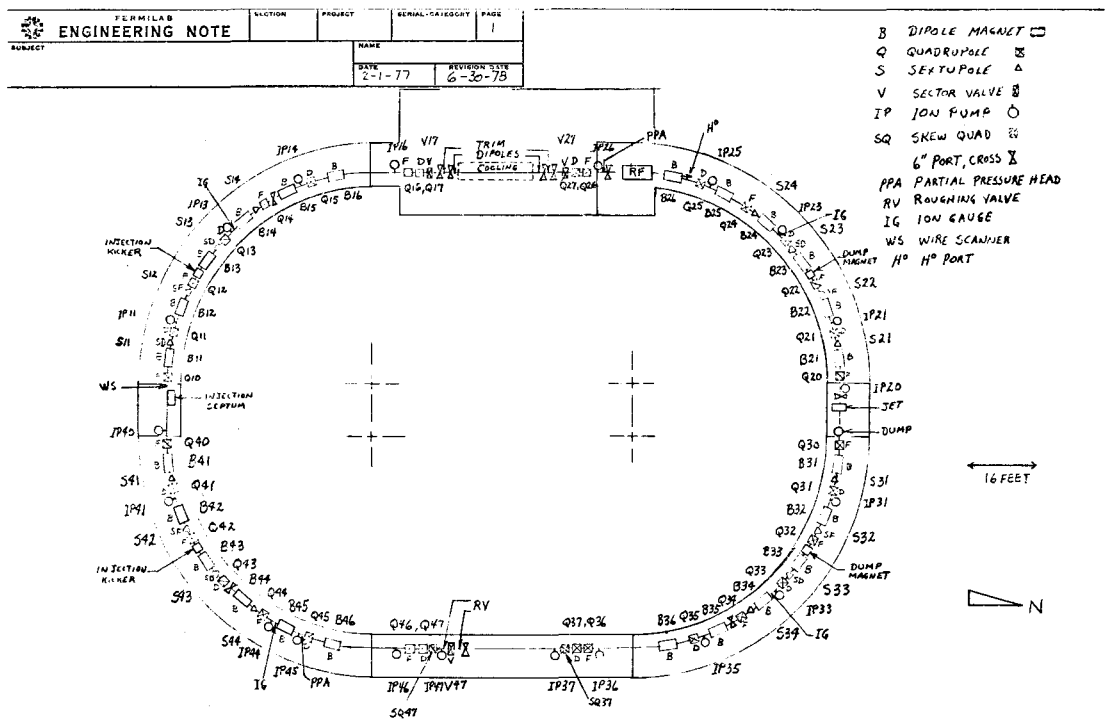

Fig. 13 Cooling Ring Lattice

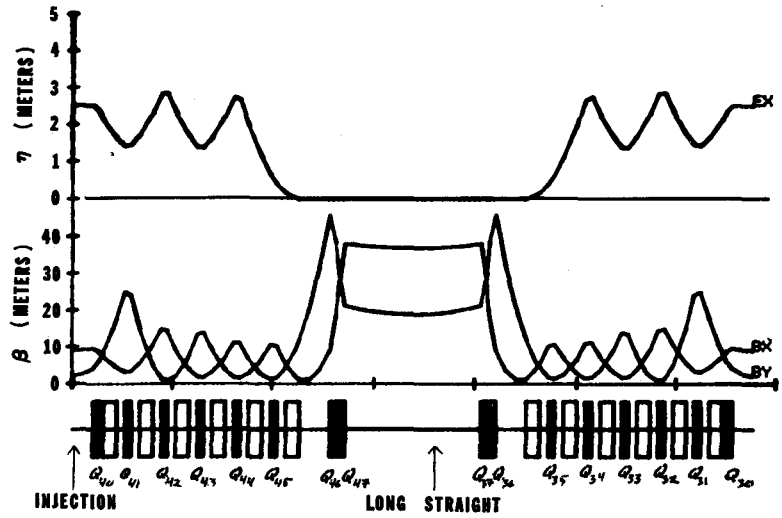

Fig. 14 Racetrack Superperiod

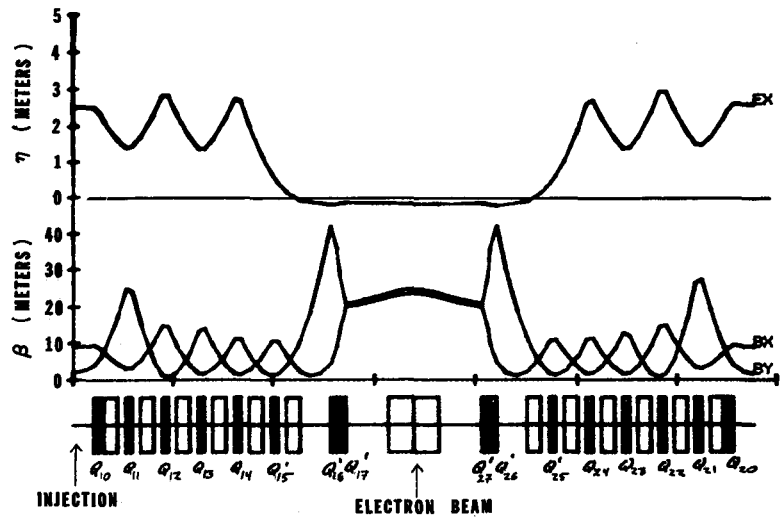

Fig. 15 Half Racetrack with Cooling Straight Section

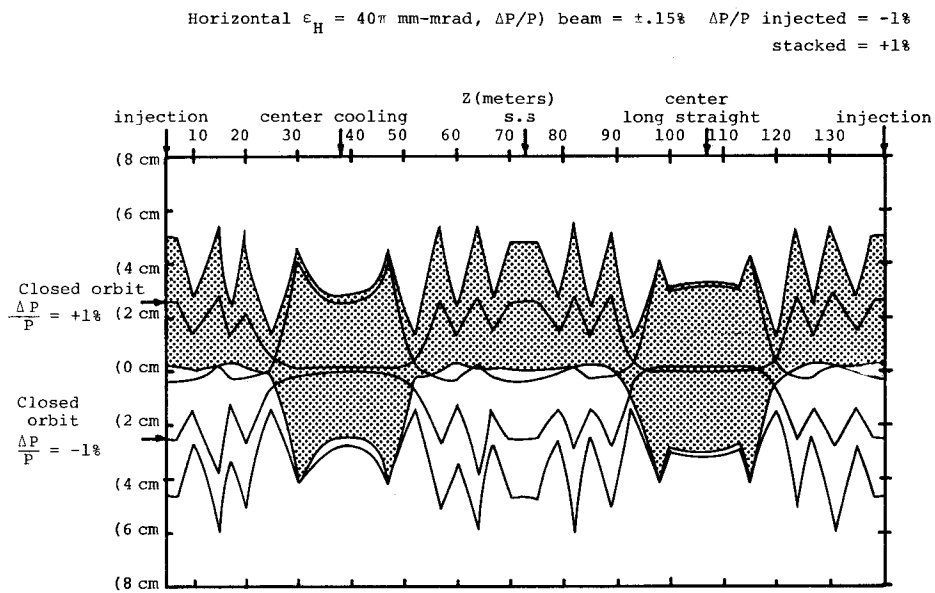

Fig. 16 Proton Cooling Ring Injected and Stacked Beams with e^- Beam

Fig. 17 Vertical Beam Size

$\varepsilon_v = 20\pi$ mm-mrad

Table I

Initial Design Lattice Parameters

1. General

Momentum	645 MeV/c	
Corresponding bend field	4.29 kG	
Magnetic bend radius (ρ)	5.01 m	
Radius	21.56 m	
	= 24/84 Booster radius	
Revolution time	~798 nsec	
Number of Periods:		
without electron beam	2	
With electron beam	1	
Focusing structure	separated function	
	FODO normal cell	
	without electrons	with electrons
Nominal working point	ν_H = 3.68	3.69
of stacked orbit:	ν_V = 5.42	5.42
	γ_T = 3.68	3.69
Chromaticity	ξ_H =-1.01	- .82
after correction:	ξ_V =-1.86	- .74

2. Magnets

Number of dipoles	24
Length of dipoles	48.00"
Effective dipole length	51.52"
Number of quadrupoles	32
Length of quadrupoles	24.00
Number of sextupoles	16

Quadrupole gradients, $\Delta p/p = 0$:

$Q_{10}, Q_{20}, Q_{30}, Q_{40}$	7.41 kG/m		
Q_{11}, etc.	-14.66		
Q_{12}	14.66		
Q_{13}	-17.60		
Q_{14}	17.60		
Q_{15}	-19.35	Q_{15}'	-16.99
Q_{16}	20.95	Q_{16}'	20.34
Q_{17}	-19.93	Q_{17}'	-19.67

Sextupole strengths:

$(B''\ell)_F$	5.69 kG/m
$(B''\ell)_D$	-10.71 kG/m

3. <u>Structure</u>

A. Curved section

Elements in curved section	Length
Bending Magnet (B)	4 ft
Quadrupole (Q_n)	2 ft
Drift Space (0)	3 ft

Cell structure: (QF)0(B)0

(QD)0(B)0

Cell length 24 ft

B. Short Straight

Injection Drift Space (SS)	6 ft	5.91 in
Short Drift Sapce (00)		18.00 in

C. Long Straight

Drift Spaces (D16A)	10 ft	0.08 in
(D16B)		10.00 in
(LS)	22 ft	2.44 in

D. Quadrant Structure: (Q)

SS(Q10)00(B)0(SD)(Q11)0(B)0(SF)(Q12)

0(B)0(SD)(Q13)0(B)0(SF)(Q14)0(B)

0(Q15)0(B)D16A(Q16)D16B(Q17)LS

Complete Structure: $Q(\bar{Q})Q(\bar{Q})$

Total length of extraction orbit 135.4865 m

444 ft 6.11 in

4. Apertures and acceptances

Mominal vacuum chamber aperture: $a_H = \pm 76$ mm

$a_v = \pm 25$ mm

Sagitta 42.9 mm

Available aperture $a_{H_{tot}} = \pm 54.6$ mm

Lattice Functions: (a) without electron beam, $\Delta p/p = 0$

	Maxima	In dipole	L.S.	S.S.
β_H	45.55 m	11.88 m	18.88 m	9.00 m
β_V	37.99	17.67	36.75	2.00
η_H	2.84	2.33	0.00	2.50
(b) with electron beam, $\Delta p/p = +1.0\%$				
β_H	44.81	12.36	23.88	7.75
β_V	35.97	18.67	25.22	1.61
η_H	2.96	2.42	-0.23	2.49

Acceptance (using beam size in dipoles)

$a_{H\beta} = \pm 21.8$ mm $\qquad \varepsilon_\pi = 40\pi$ mm-mrad

$a_{Hp} = \pm 3.4$ mm $\qquad \Delta p/p = \pm 1.5(10)^{-3}$

$a_{H_{tot}} = \sqrt{a_{H_\beta}{}^2 + a_{H_p}{}^2} \qquad = \pm 22.1$ mm

$a_v = \pm 18.8$ mm $\qquad \varepsilon_v = 20\pi$ mm-mrad

Angles in L.S.:

$\theta_\parallel = \sqrt{\varepsilon/\pi\beta_{L.S.}} \qquad \theta_H = 1.3$ mrad

$\theta_\perp \sim \gamma\ \Delta p/p \qquad \theta_v = 0.9$ mrad

$\theta_\perp = 1.8$ mrad

The natural chromaticity of this machine will be nearly cancelled over a large range of momentum variation by the addition of two families of sextupoles, having a maximum integrated field of about 10 kG/m. Figs. 18 and 19 show graphs of the tune variations vs. momentum deviation for

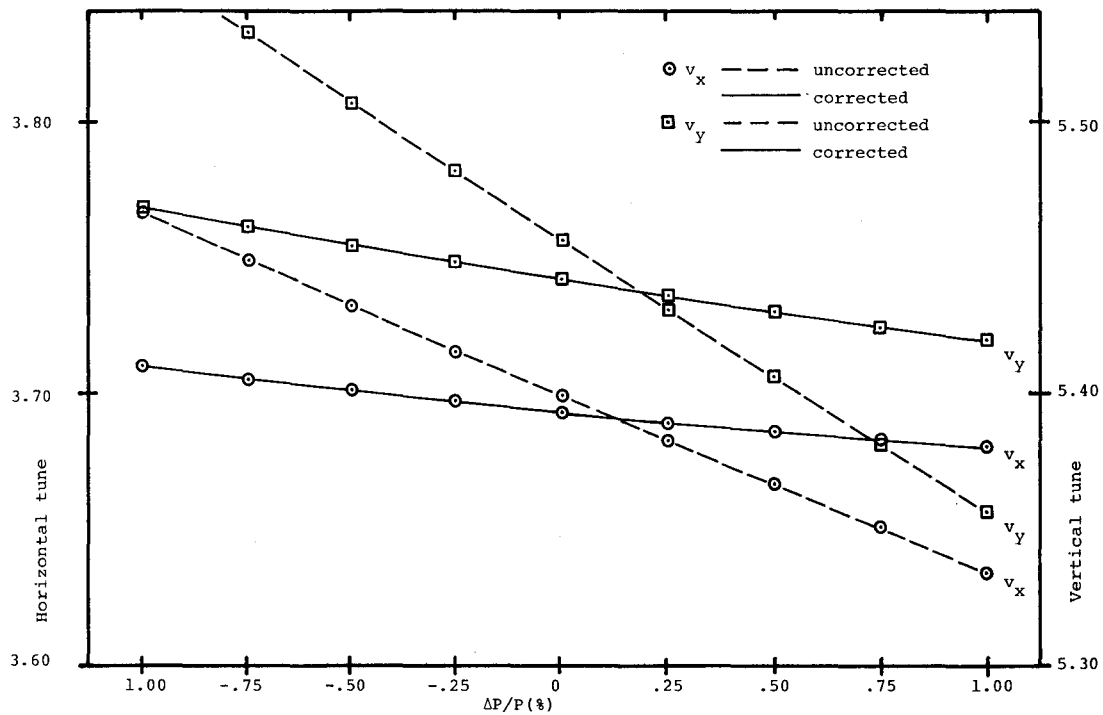

Fig. 18 Tune vs. ΔP/P Without Electron Beam

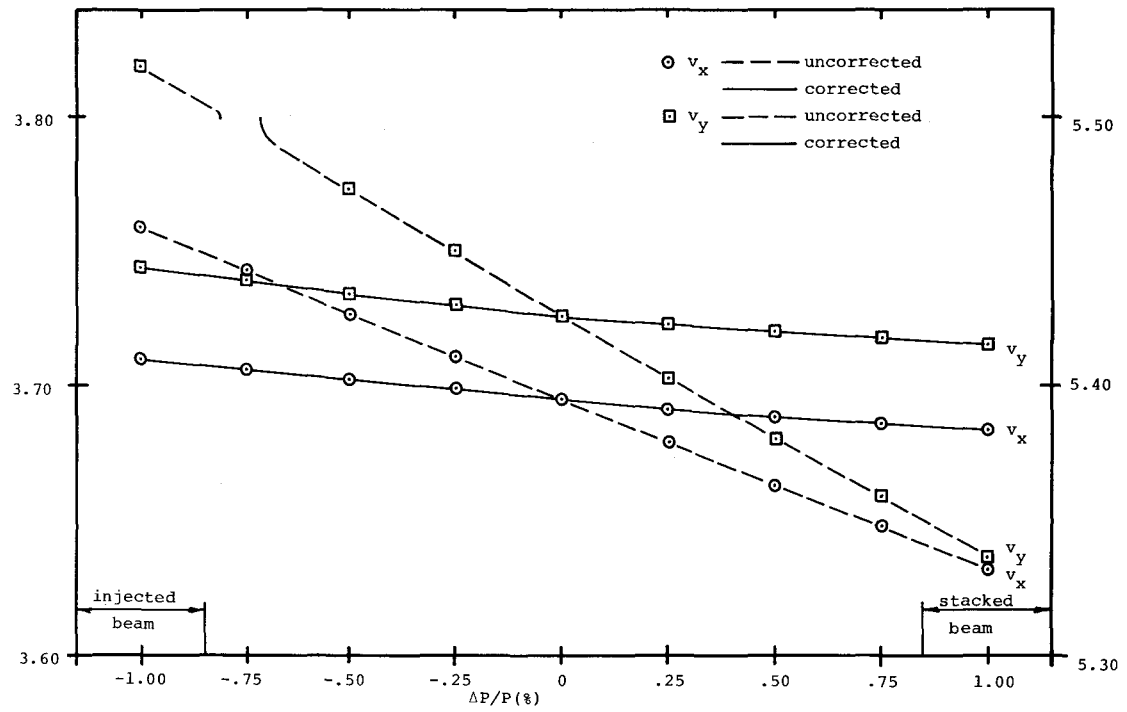

Fig. 19 Tune vs. ΔP/P Electron Beam

both of the initial designs. Plotted are the tune variations for the natural chromaticity as well as those after the chromaticity has been reduced with the two sextupole families mentioned above. In the "corrected" case, the final chromaticity, at the stacked orbit of $\Delta p/p$ = +1%, has been adjusted so as to be slightly negative in order to prevent beam instabilities, negative as we are below transition gamma. Figure 19 also shows the relative momentum region to be spanned, approximately 2% between the injected and stacked beams, and ±.15% across the beam. Figure 20 is a normal tune diagram showing the region covered by the beam while transversing this momentum range, and finally, in Fig. 21 is plotted the horizontal dispersion function, η, at the center of the cooling straight section, linearized around the closed orbit, for the uncorrected cases. This is important as it effects the rate of the electron cooling.

The tunes have been chosen so as to be well away from any major resonances. The only resonance half-width of significance comes at the tune $3\nu_x = 11$. There could be three contributions to this line, but they are all quite small. The contribution due to the addition of the two sextupole families is very nearly zero because the lattice, even with the fully unneutralized electron beam, has essentially a superperiodicity of two. The contribution from the electron beam itself, along with associated end effects, solenoid and toroid fields, etc., has been shown to be a skew field,[4] and so does not effect this resonance. Also, there is an increase in its width due to random sextupole error in the dipoles. This has been calculated to be less than $\Delta\nu = .007$, which should cause no trouble. Finally, the half-integer stopband width due to gradient errors were calculated and found to be

a. for a systematic gradient error in dipoles

$$\Delta\nu = 3.169\ (B'/B)$$

b. for a systematic quadrupole error

$$\Delta\nu = 13.6\ (\Delta B'/B')$$

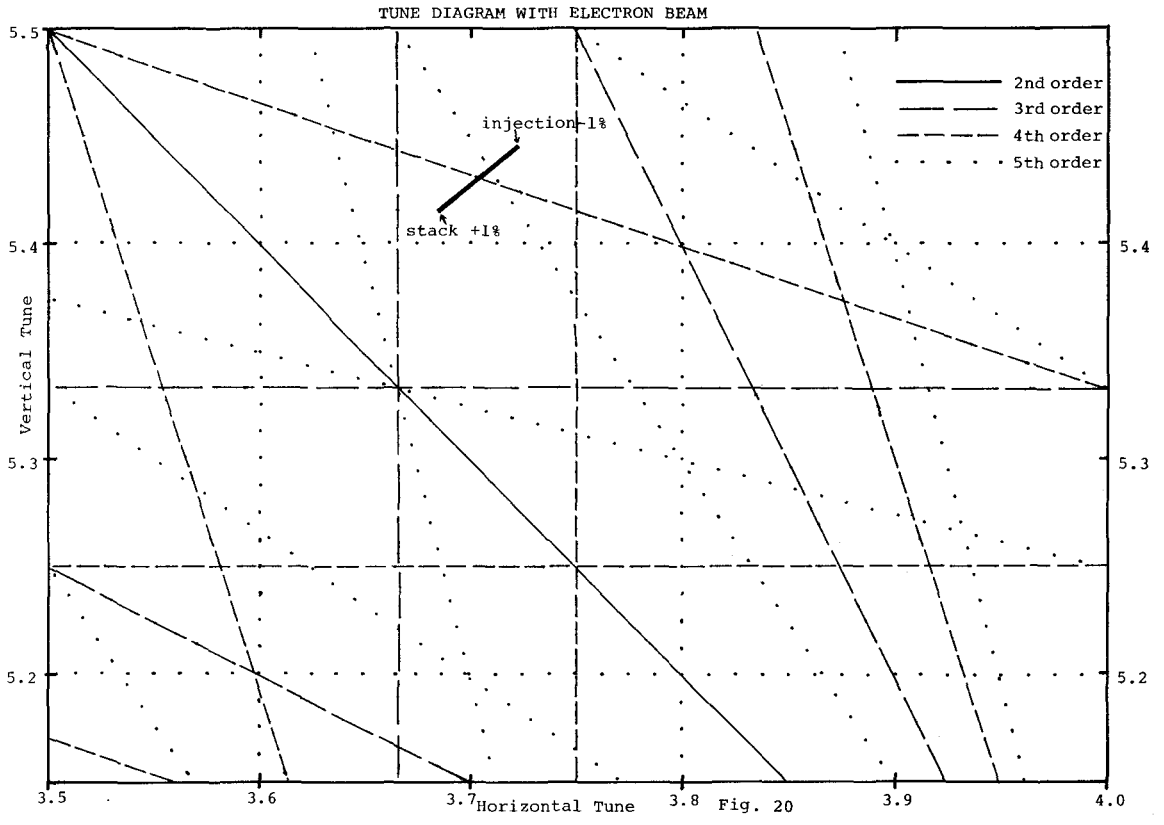
TUNE DIAGRAM WITH ELECTRON BEAM
2nd order
3rd order
4th order
5th order
injection -1%
stack +1%
5.5
5.4
5.3
5.2
Vertical Tune
3.5
3.6
3.7
3.8
3.9
4.0
Horizontal Tune

Fig. 20

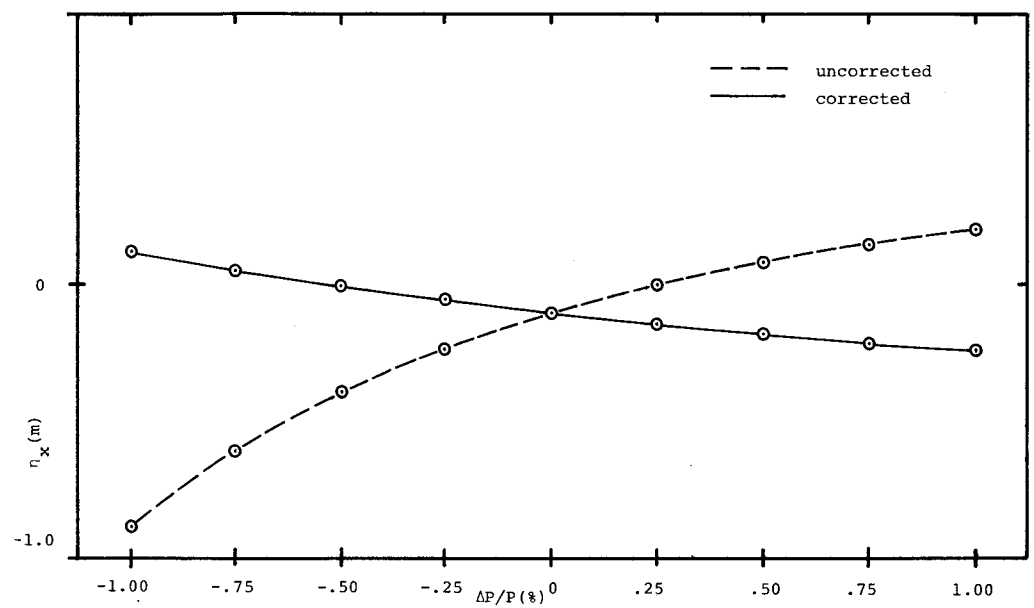

Fig. 21 Dispersion in Center Cooling Straight vs. $\Delta P/P$

c. for random quadrupole error

$$\Delta\nu = 4.8\ (\Delta B'/B')_{rms}$$

B. Antiproton Ring in Booster Tunnel

A design using these magnets which fits into the present booster tunnel has been briefly examined. It has, of necessity, 12-fold symmetry and has been taken to have superperiod 12. It is also the simplest design possible, using only the minimum number of dipoles and quadrupoles. Lattice functions for this design are shown in Fig. 22 and the basic parameters are listed in Table II.

C. Above Ground Booster Length Ring

There is one further possibility - that of converting the initial racetrack design into a structure of booster circumference. This could be done either by telescoping the present design along its length, or remaking it into a true four-sided figure. Either method would be possible by the addition of many dipole-free normal cells. This however, would require the addition of some 90 quadrupoles, and so is not a very pleasant choice. Although no detailed design currently exists, one can devise matching straight sections of the proper lengths using considerably fewer additional quadrupoles to connect onto the present curved sections. In attempting to expand the present racetrack, the southern end cannot easily be moved further south due to presents of access road, waterworks, etc. In addition, if all of the extra length were taken up by the northern end, the lattice would run nearly into the H^- injector pit. Thus, one would possibly go to a more nearly square geometry, perhaps with superperiod 2 or 4.

References

1. D.E. Johnson, "Proton Cooling Ring Lattice Design Including Electron Beam Tune Shift", 1977 Aspen Summer Study.

2. G. Guignard, M. Month and W.T. Weng, "The Electron Space Charge and Solenoid Field Effects on the Proton Cooling Ring", 1977 Aspen Summer Study.

3. B. Autin and G. Guingnard, "End Effects of the Cooling Section on the Proton (Antiproton) Beam", 1977 Aspen Summer Study.

4. A.G. Ruggiero, private communication, December 1977.

Table II

12-Sided Ring

Regular, 12-sided polygon	12 x 40.4 meters
straight sections (free)	12 x 17.2 m
Energy	200 MeV
Magnets:	24 4' dipoles @ 4.6 kG
	60 2' quadrupoles @ ~15 kG/m
Superperiod	12
ν_x	7.85
ν_y	5.85
β_x^* (cooling region)	40 m
β_y^*	25.6 m
η^*	2.97 m
η'^*	0
β_x max	41.9 m
β_y max	49.6 m
η max	2.97 m
No. of quadrupole supplies	3

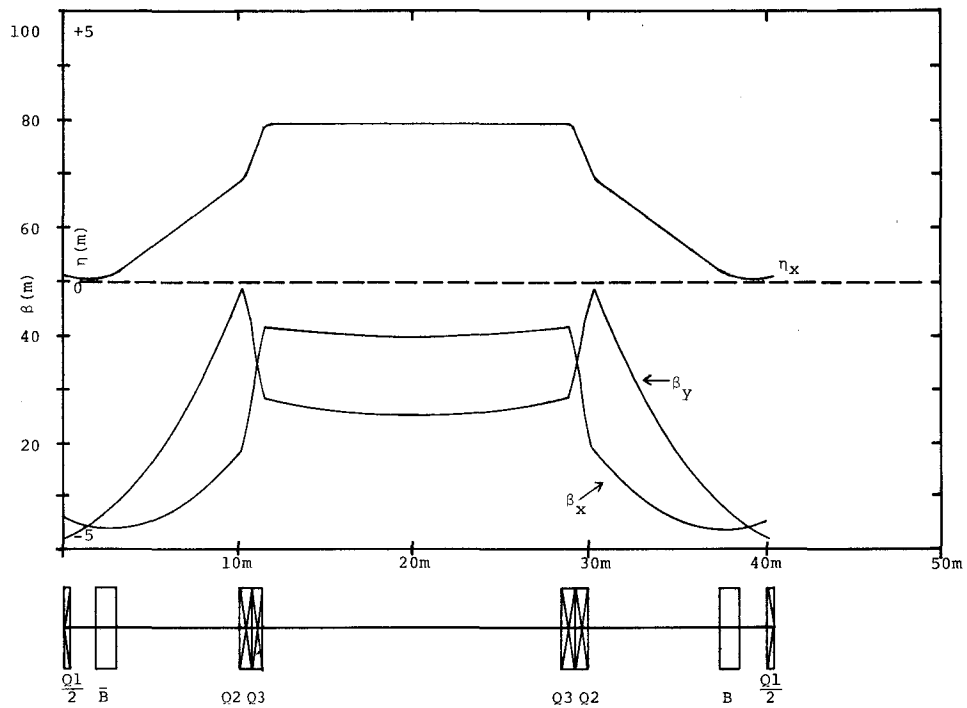

Fig. 22 Booster Cooling Ring Lattice Functions

V. Magnet System

The symmetric lattice discussed in Section IV is composed of 32 quadrupoles and 24 dipoles. Asymmetric lattices have been studied which also require 32 quadrupoles.

Dipole Magnets

For reasons of economy and ease of construction, the dipole magnets were chosen to be straight in spite of their large bending angle. The four foot length yields an acceptable (1.6") sagitta and field (0.5T). The vertical aperture is sufficient to accommodate 20π μrad acceptance, 1/8" vacuum chamber walls, heater cables and ½" insulation for in situ vacuum baking. The radial aperture is sufficient to contain two 40π μmrad beams separated by $\Delta P/P = 2\%$ at all points in the lattice, the 1.6" sagitta, 1.5" wide pumping elements on both sides, chamber walls and insulation. The pumping elements are located in fringe fields unacceptable for particle motion.

The magnet was chosen to be a modified picture frame magnet with a small pole. This gives a smaller current density and locks the coil in place. There is no other coil restraint. A Rose shim is employed to extend the good field region to within one half gap from the coil.[1] Figure 23 gives a cross section of the magnet.

The magnet is fabricated of two laminated half-cores clamped together by 26-3/8" bolts. The laminations are stacked in a fixture together with the end plates, being clamped after each 6" of laminations. Laminations are alternated in direction each 2" in order to remove any asymmetry caused by the die or by remanence due to rolling direction. The core is welded, while clamped, to a let-in key and to let-in angle irons which are used to clamp the two cores together. Length variations were kept less than one lamination.

The 1" end plates are fabricated of normal laminations glued together with epoxy. A bevel is machined at 30° to the pole surface to terminate the magnetic field without saturation. The bevel is machined in steps to achieve uniformity of magnetic field length across the radial

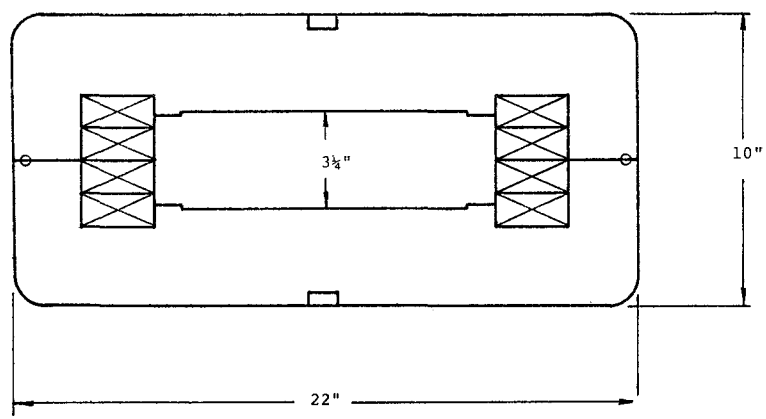

Fig. 23 Dipole Magnet Cross Section

aperture. Delamination of the glued end plate occurred in several cases, causing a field integral variation of $\sim 7 \times 10^{-5}$, and was repaired by re-gluing and stainless steel screws. Longitudinal grooves on the mating surfaces accepted a 3/16" drill rod to register the two half cores in the horizontal direction. It was found that the corner of the lamination was drawn up by the welding and produced an apparently large back leg gap in this region, but no obvious deterioration of magnet performance resulted.

During early production measurements, it was found that the magnets were not reproducible after disassembly and reassembly. This was solved by tightening the clamp bolts near their tensile limit and further squeezing between them with a C-clamp to the same stress level. After this treatment, all magnets tested reproduced to about one part in 10^4. The local stress placed on the lamination surfaces was equivalent to ~500 tons total on the mating surface. This is approximately ten times the magnetic force at normal fields. The final clamping stress was 40% of the maximum.

The coils ends are bent at 45° to clear the vacuum chamber. The coils were wound on a rocking fixture on a carousel. It was found that the work hardening of the copper due to this bend gave enough strength to support the coil end. An automatic tension mechanism was employed to assure straightness. Each half coil is composed to two double pancakes of five turns giving 20 turns per half coil. The coils were insulated after winding with polyester tape and each pancake was wrapped. Pancakes were separated with 1/16" G-10 insulation; the half coil was surrounded with G-10 and wrapped again. Each pancake is a separate water circuit with ~65 psi pressure drop.

The magnets were corrected empirically by machining the end plates 1/16"deeper over the central 6" and adding a 1" shim 1/16" thick at each pole edge. The effective magnetic length of the dipole is 51.52". The magnets have a slightly concave field distribution at a level of 1-2 parts in 10^4 over an 8" aperture. In Fig. 24 we show the field in the central region of the magnet and a field integral of a typical magnet as a func-

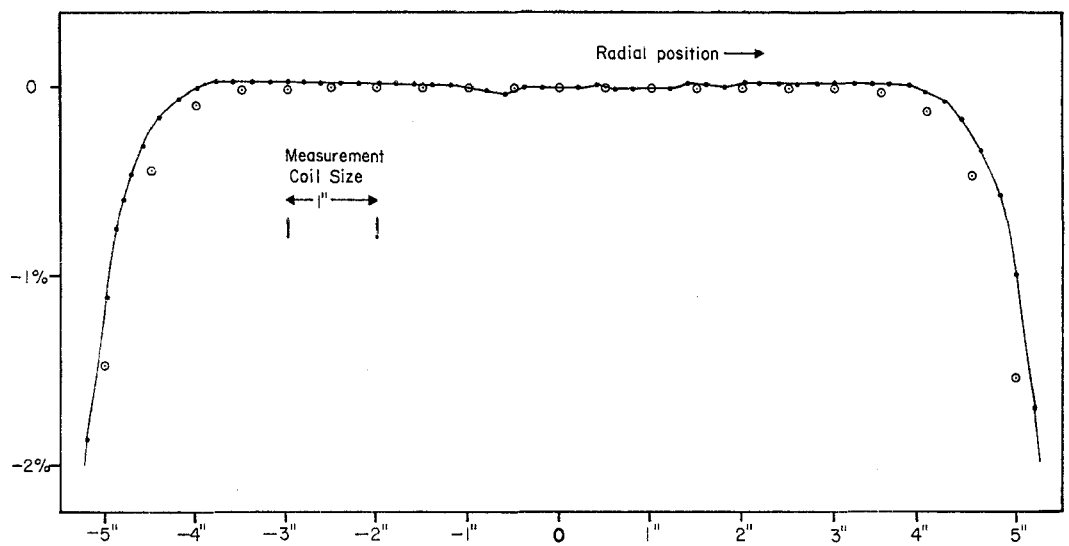

Fig. 24 Variation of $\int B\,dl$ in Dipole

Measured Field in Magnet Center (Magnet 1002)

Measured Integral (Magnet 1005)

tion of horizontal position. The integral is made with a 1" wide coil and no correction is made for width of coil. The rms deviation of the central field integral for all magnets fabricated was 7×10^{-4}. This is consistent with length control during stacking. This error is sufficiently large that the magnet locations were chosen to minimize closed orbit errors by distributing the error in a low (principally 1st) harmonic pattern in the ring. The maximum closed orbit error due to the measured errors is calculated to be 2 mm. Magnet twists are determined optically, and are as large as 3 mrad. Five measurements of twist were made on each dipole. These were averaged and adjusted by survey to a level of approximately 1/3 mrad. This will contribute about 1 mm of closed orbit error.

Quadrupole Magnets

The quadrupoles are rather weak; ~.5 kG/in nominal and 24" long. The 6 1/2" bore is sufficient to contain a 6" beam pipe and allow insulation for bake out. The general construction features of the quadrupoles are similar to those of the dipoles. Extra steel was stamped into the back legs of the laminations to avoid oil-canning. The laminated end plates were made 1½" thick to resist bowing of the salient poles. The problem of reproducibility after disassembly and reassembly was not as serious as in the dipoles.

The coils are double layer solenoid-wound. They were insulated with polyester tape before winding, insulated with G-10 and ground wrapped. It was determined that the tape retained its rated insulation value after bending through a minimum 1" radius of curvature. The cross sections of the quadrupole lamination and coils are shown in Fig. 25. The coils on a half core constitute a single water path at 65 psi.

Correction was achieved empirically, and resulted in a flat beveled surface at 30° to the pole penetrating 5/8" into the end. The measured gradient integral and calculated central gradient are shown in Fig.26. The gradient integral coil is 1" wide and ½" high. No correction has been made for finite coil effects. The remaining error is predominantly 20-pole in form ($B' \sim x^8$). Only in the injection straight section quads,

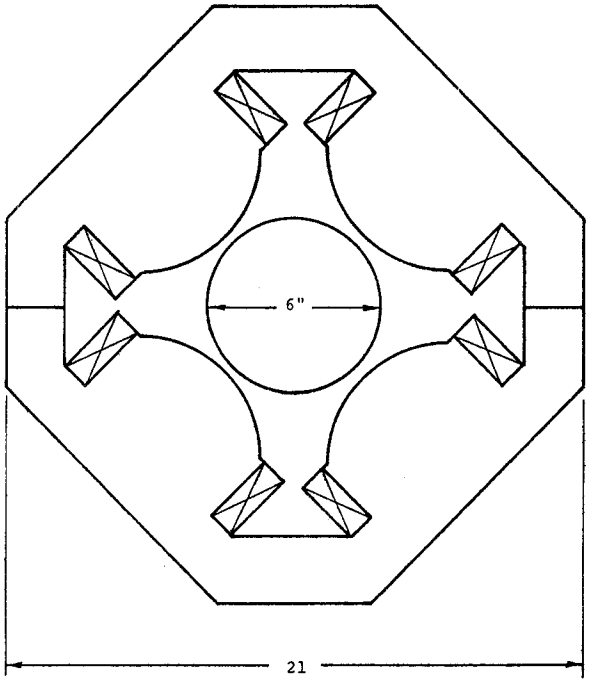

Fig. 25 Quadrupole Magnet Cross Section

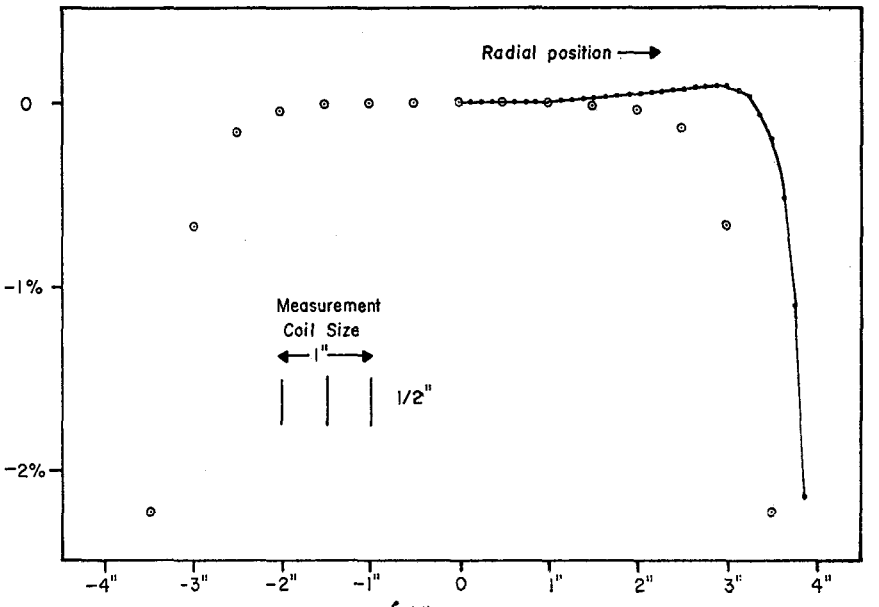

Fig. 26 Variation of $\int B'dl$ in Quadrupole

Computed for center of Quadrupole

⊙ ⊙ ⊙ Measured Integral (Magnet 1037)

where three beam regions exist side by side, are these errors of concern. Analysis has shown that these errors create negligible stop bands for resonances in the neighborhood of the working point.

The central gradient integral variation for all 38 quadrupoles produced was 7×10^{-4}, for those chosen for the ring, 5×10^{-4}. Since there are nine quadrupoles buses, it was possible to choose the quads for each bus to vary by less than 2×10^{-4}. The effective gradient length of the quadrupoles is 26.64".

Reference

1. Private communication, Stanley C. Snowdon.

Table III

Cooling-Ring Dipole

Field Strength	4.3 kG
Magnet length	48 in
Magnet gap	3.25 in
Coil Aperture	12"
Field Aperture	±4.00
Field quality ($\Delta B/B$ within 3 in.)	$\pm 10^{-4}$
Coil turns (top and bottom)	40
Copper conductor cross section	0.46 in. by 0.46 in.
Water cooling hole diameter	0.25 in.
Conductor corner radius	0.063 in.
Conductor current	711A
Magnet Inductance	0.010h
Coil Resistance	0.025Ω
Voltage drop	17.8V
Power	12.6 kW
Cooling Water pressure	65 psi
Number of water paths	4
Water flow	4.4 GPM
Temperature rise	13.1°C
Outside dimensions	10 in. by 22 in.
Iron weight (approx.)	2100 lb
Copper weight	288 lb

Table IV

Cooling-Ring Quadrupole

Field gradient	0.50 kG/in.
Magnet length	24 in.
Aperture	6.5 in.
Width of good field gradient	±3.0
Gradient quality	.5%
Coil turns per pole	10
Copper conductor cross section	0.46 in. by 0.46 in.

Table IV

Cooling-Ring Quadrupole (continued)

Water cooling hole diameter	0.25 in.
Conductor corner radius	0.063 in.
Conductor current	535A
Magnet inductance	1.75 mh
Coil resistance	0.0132Ω
Voltage drop	7V
Power	3.8 kW
Cooling water pressure	65 psi
Number of water paths	2
Water flow	2 gpm
Temperature rise	$7^{o}C$
Outside dimensions	21 in. by 21 in.
Iron weight	1590 lb
Copper weight	140 lb

Table V

Lattice Specifications

Dipoles	
Number of magnets	24
Total current	710 Amps
Total voltage	460 Volts
Total power	325 kW
Number of power supplies	2 (in series)
Quadrupoles	
Number of magnets	32
Total power	53.2 kW
Number of power supplies	9
Number of buses	9

VI. Cooling Ring Vacuum System

Vacuum system requirements for cooling and storage of protons (or antiprotons) indicate a need for a vacuum level of 10^{-10} torr. Since this is below the normal lower limit (of order 10^{-8} torr) for unbaked conductance-limited chamber, a bakeable system is required. The magnet design has necessitated a captive vacuum chamber which requires unbolting the magnet halves for removal and therefore, a need for in-situ baking. Strength and ease of welding considerations give a preference to stainless steel. Aluminum is of less interest because the radiation problems of electron machines are not present.

Many designers have come to the conclusion that distributed ion pumps not only put pumping where it is needed, but also give a lower cost per unit pumping speed than lumped pumps. The present magnet design has field regions along the beam aperture that are useable for distributed pumps.

With these requirements, the basic design parameters of the vacuum system can be summarized as:

a) Stainless steel

b) All welded

c) In-situ baking

d) Distributed pumping

The cooling straight section has unique problems and is treated separately.

A. Baking System

Reported outgassing-rate measurements for stainless steel seem to indicate the need for a higher temperature bake for stainless steel than is required for aluminum. A design in-place baking temperature in the range of 400°C was chosen. Higher temperatures strain the materials used for heating and insulation and lower temperatures are not as effective. A vacuum bake prior to assembly in excess of 900°C is also needed to remove hydrogen from the bulk metal.

Even at 400°C, the insulation materials to be used are limited. The thermal conductance (K factor) of a ceramic fiber insulation that is readily available is 0.72 BTU-inch/sq. ft-hour-°F, a value similar to those for lower temperature materials. Using this value the estimated power required for various insulation thicknesses to maintain 400°C inside a 50°C magnet for the entire ring (24 dipoles, 32 quadrupoles) is given in the following Table:

Table IV. Baking Power Required

Thickness (in.)	Power (kW)
1/8	634
3/16	422
1/4	317
5/16	254
3/8	211
7/16	182

Since this material is available in 1/2-in. thicknesses and is readily compressible, a 1/2-in. thick insulation compressed to 3/8 in. at heater elements is selected as an optimum value. Heater tape is the most straightforward heating method. Wrapping the tape around the chamber insures some uniformity of temperature (a necessary feature). On the other hand, reliability of heater tape at these temperatures has been found to be too low to use in the captive dipole chambers. With replacement difficult in the dipoles, a design with somewhat more expensive heater cable has been made. The lifetime of this cable, when it is used properly, is long enough that no problem should occur. Normally accessible places, such as straight sections, for example, will still be heated with tapes. Since even the most expensive sector valves cannot be baked closed at 400°C, a lower temperature limit will exist at closed valves. The initial bake should cover the whole ring to take advantage of the higher temperature limit of open valves.

Heater power will be from the same transformer used for the magnet power supplies.

B. Vacuum Chamber

The chamber for the quadrupoles and straight sections is 6-in. diameter type-304 stainless steel wrapped with heaters and ceramic fiber insulation in a straightforward manner.

The chamber for the dipoles is less obvious. The basic free area desired for the beam is 2 x 7 in.^{2}. Adding approximately 1.5 in. on each side for distributed ion pumps give a chamber of approximate dimensions 10 x 2 in. Figure 27 is a full-scale drawing of one half the chamber; the other side is a mirror image. Stress calculations for this rectangular shape, assuming that the screen between the ion pump and beam region is a vertical support, indicate a maximum stress for 1/8-in. walls of about 20,000 psi. The yield point for type-304 stainless drops about 40 percent from room temperature to 400°C, putting it at the 20,000 psi value. Wall thickness must therefore be no less than 1/8 in. Drawing seamless pipe to this shape and size is too difficult. Inserting the screen and supports from the ends also complicates such a design. Two flat pieces, each bent at both sides to form a flat U-shape and then welded with a full penetration weld at the center of the sides provide the simplest construction. The weld would thus not be at the corners, the point of maximum stress. A prototype chamber was measured to flex about 50 mils in the center in close agreement with calculations.

The screen supports are necessary to support the chamber, but since the magnet design is straight and the beam enters and exits at an angle, it is desirable to remove the screens at the ends. The support on the inside of the ring is shorter and the outside support is bent toward the ring center for support. This allows a full 6-in. aperture, even with the beam sagitta.

The center-to-center distance between magnets in the ring is 6 ft and approximate chamber lengths of 6 ft for the dipoles and the quadrupoles are convenient. Each end of a dipole chamber is cut at the half angle of the magnet bend and has a flat plate welded to the chamber. Connection is made to a 6-in. round chamber at this plate. This construc-

tion appeared to be the least expensive method.

A significant problem is the thermal expansion of about 1/2 in. per 6-ft section of vacuum chamber at the 400°C bake temperature. This expansion must be taken up by bellows. For simplicity, bellows will be put only in the round chambers. This means that allowance for a radial-movement component of 33 mils in the round pipe at the angle change of the bend magnet chambers must be included.

Floor supports will be used to hold the insulated vacuum chamber in the straight sections and a simple standoff support will position the chambers relative the magnet yoke on the side interior to the ring.

C. Roughing System

The overall ring is divided by three sector valves into two pieces plus the cooling straight section. These valves are all metal bakeable open to 400°C. Each half of the ring has a volume of 38 ft^3. A roughing chamber sets astraddle to the sector valve in the long straight opposite the cooling straight. This chamber has a valve to each half of the ring. This will allow roughing and rebake of each half of the ring separately. Attached to the roughing chamber is a magnetic bearing totally oil free turbomolecular pump with a trapped mechanical pump. The turbo will allow in place bake to occur in the 10^{-5} to 10^{-6} torr range.

D. Ion Pumps

A suggested realistic outgassing rate for the walls of a large stainless steel chamber is 10^{-12} torr-liters cm^2-sec^1. Using this number for the ring, which has an estimated surface area of 7.8×10^3 cm^2 and a desired pressure of 10^{-10} torr, required pumping speed of 7800 ℓ/s at 10^{-10} torr.

Figure 27 shows the dipole chamber with distributed ion pumps on both sides of the beam aperture. The pump design is basically a variation of a Physical Sciences Laboratory (University of Wisconsin) design with five sections that are 2 cells wide by 27 cells long. Two sections are on the inside ring side and three on the outside. The pumping speed per dipole was estimated to be approximately 200 ℓ/sec at 10^{-10} torr from

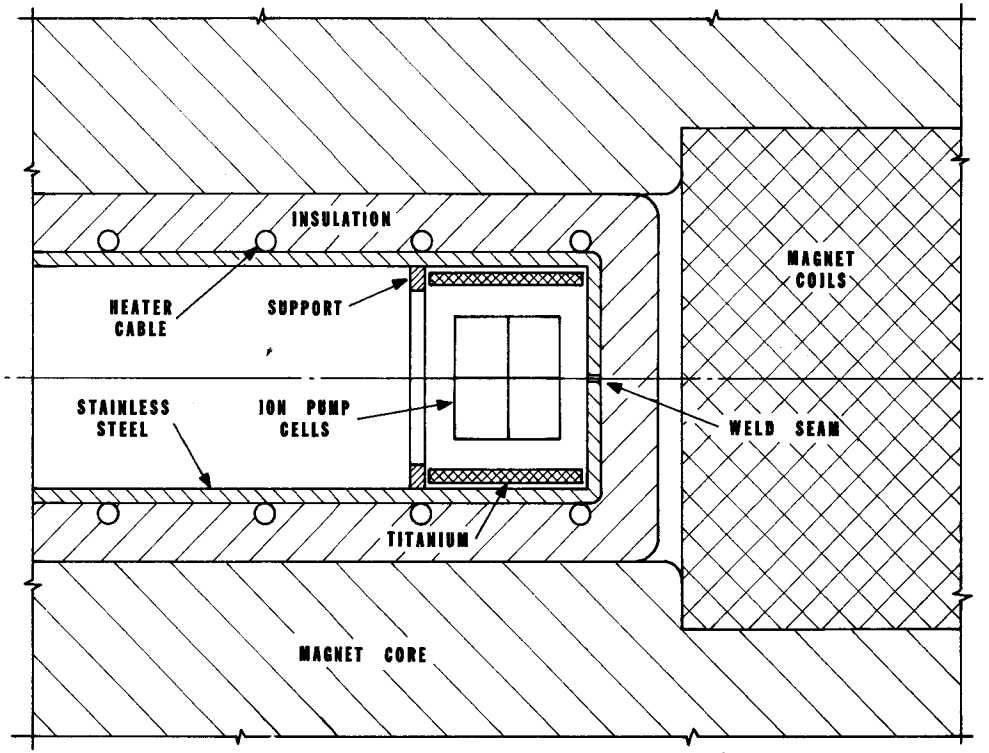

Fig. 27 Distributed Ion Pump Cross Section

higher pressure measurements. This value is less than the estimated value from early model measurements. However, the dipole chamber used for the pumping speed measurements had been vacuum degassed at 900°C for one hour below 10^{-5} torr. The base pressure observed was consistant with earlier outgassing measurements by a factor of 2 or 3 below the design valve of 10^{-12} torr liter/cm^2 sec. All the chambers in the cooling ring proper have had the high temperature degassing; so that a base pressure near 1×10^{-10} torr should be possible without additional pumping of no other gas sources are introduced.

Twenty main ring style triode pumps were added to the ring to provide pumping when the magnets are off. These pumps alone should be able to hold a pressure in the mid 10^{-9} torr range. They also provide for some inert gas pumping.

E. Miscellaneous

All devices that need to be placed in the vacuum chamber must be compatible to high vacuum and be bakeable to above 400°C. This restriction limits the materials to basically metal and ceramic. As a result, a position detector design of the capacitive cross-cut tube design has been made using five inch tubing supported by ceramic bars. Because of space limitations in the ring these detectors are placed inside all the quadrupole magnets except the two in the injection short straight.

An injection kicker design of the strip line type has also been made using ceramic bars for support. The only materials in the vacuum are ceramic, stainless steel, and OFHC copper bars.

Each quadrant of the ring has an ion gauge with an X-ray limit of less then 1×10^{-11} torr. A gauge is placed in the middle of the long straight at the maximum distance from any pumps. If the peak pressure here is too high additional lumped pumps will have to be installed.

Injection of protons from the linac will be on the inside of the south short straight through a 2 mil stainless steel window. Vacuum requirements of the injection-line are very relaxed compared to storage ring requirements.

VII. Injection and Accumulation

A. Extraction from Linac

Protons will be extracted from the switchyard area of the linac for the cooling experiments. The protons will be directed up an existing 16 inch pipe to ground level and transported to the south end of the cooling ring as indicated in Fig. 27. In the first stage of the experiment, coasting beam will be established and electron cooling will be attempted on a single pulse of reasonable intensity. After this step has been accomplished, accumulation and cooling will be done on beams of lower intensity. The beam extracted from the linac must meet several requirements for proper matching into the racetrack. These requirements are summarized in Table VII, together with some other parameters of interest.

Table VII. Injection Beam Parameters

	Tuneup	Accumulation
Momentum	644 MeV/c	642 MeV/c
Intensity	10^7/2 sec	10^7/66 msec
Filling time	800 nsec	
Linac intensity (800 nsec)	10^{12} { H^+ }	
	10^{11} { H^- }	

The beam line is shown schematically in sections in Fig. 28. and as the elements of the beam line are described, their relation to the requirements in the Table VII will be indicated.

B. Linac

The first element in the beam line is the 750-keV chopper, which is located upstream of the linac. The chopper is the device that restricts the time duration of the pulse to 800 nsec. Then the beam is accelerated normally to 200 MeV and goes through the spectrometer magnet toward the momentum dump. Emittance measurements at the beginning of the spectrometer magnet have been used to estimate the shape of the beam downstream of the spectrometer magnet. This estimate of beam size was then used to determine the necessary aperture size of three magnets that are used to pitch the beam 80° vertically and 7° horizontally. The 8° magnet

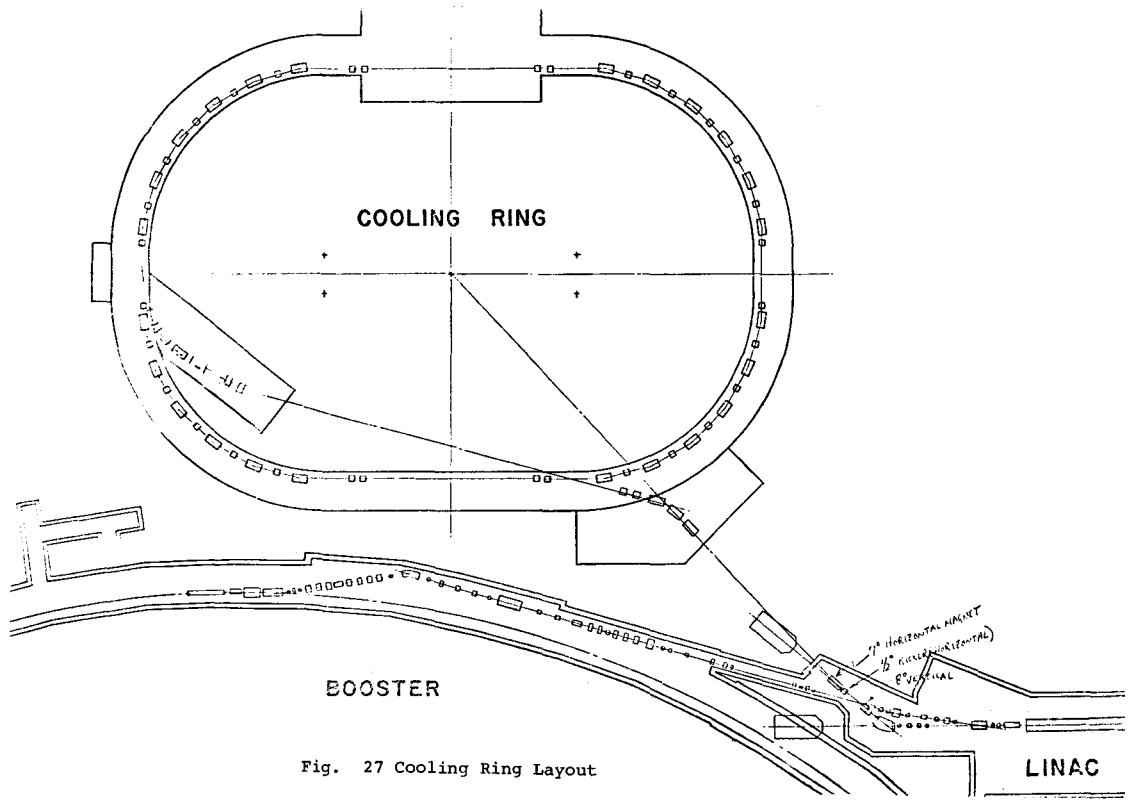

Fig. 27 Cooling Ring Layout

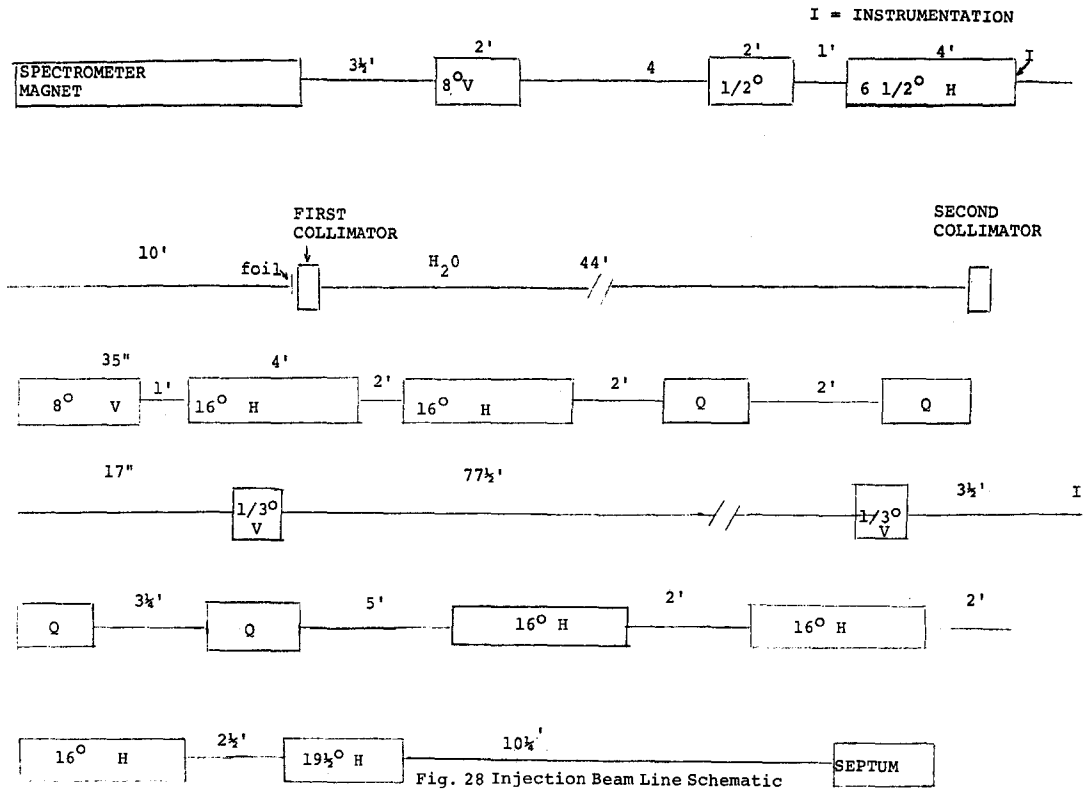

Fig. 28 Injection Beam Line Schematic

is located close to the spectrometer magnet and is ramped on when beam is desired to the cooling ring. This magnet is followed by two horizontal magnets to give a 7° bend onto the center-line of the existing 16" pipe, which carries the beam to ground level. The first of these horizontal magnets is a fast pulsed magnet (approximately $1/2^{\circ}$ bend) which, in a fail-safe manner, deflects the beam onto the center-line of the 16" pipe for safety purposes. This pulsed magnet is followed by a 6.5° magnet to complete the horizontal bend. The 6.5° magnet will be one of the cooling ring dipole magnets, because it has the necessary aperture.

C. Collimation System

During H^- operation, currents of approximately 20 mA are anticipated and during normal proton operation, currents of 200 mA are expected out of the linac . Coupled with the 800-nsec duration of the pulse, this leads to intensities of 10^{11} and 10^{12}/pulse. In order to reduce the intensity, collimators will be installed in the existing 16" pipe. In order to make a further reduction to the level desired for accumulation, a scheme has been developed utilizing the length of the beam pipe. The scheme entails imposing a multiple-scattering foil upstream of the first collimator; the increased angular divergence of the beam impinging on the second collimator will cause the desired reduction in intensity. Since the exact intensity of the H^- scheme is as yet uncertain, it is desired to have a set of foils for insertion. The multiple scatterer is upstream of the collimator in order that the foil-handling system can be in air rather than in vacuum. A preliminary design has the drive motor located on the wall of the linac switchyard area and the foils located on a flexible strip threaded into the beam pipe. The window at the end of the vacuum in the pipe are made of very thin titanium for two reasons; to prevent the window from melting and in order for the multiple-scattering scheme to work, the relative difference in multiple scattering needs to be large between the no-foil and the foil case. The collimator that immediately follows the scattering foil is made of aluminum. The pipe following this collimator is filled with water, which serves two purposes;

to serve as a heat sink for the collimator, and to serve as a neutron shield against neutrons that would stream up the pipe. There will be temperature sensors in the dump to monitor the heat rise. The final collimator is used as a part of the intensity-limiting scheme and also as the device that ensures that we have a small emittance. Since the performance of this system will depend upon the shape and intensity of the H^- beam, the collimators are being designed with inserts so that the size of the slits may be varied.

D. Ring-Level Beam Line

The level of beam instrumentation is based upon the fact that one does not need good vacuum in this line and, in fact, one can have short breaks in which detection equipment can be inserted. The first such break will be immediately after the second collimator and tuning of the line in the tunnel (8° vertical, 7° horizontal, rms foil) will be done as a function of intensity at this point.

The beam will be bent flat vertically immediately after the second collimator at an elevation below the cooling ring elevation. After being bent 32° horizontally the beam then passes under the cooling ring vacuum pipe and is brought up to the cooling ring elevation via. a vertical dogleg by using two small ($1/3^\circ$) trim magnets.

There will be a total of 6 horizontal bending magnets arranged to give an S-shaped curve which has a final angle of approximately 7° coming into the septum located in the south straight section. The bend magnets all bend at approximately 16° except for the last bend which is at $19\frac{1}{2}^\circ$. Instrumentation will be placed before the last two quadrupole magnets. A tentative decision is to use a Fermilab type-D multiwire chamber at this location.

Because of the physical length of the line, provision has been made for four quadrupoles to match into the ring. A doublet has been assigned to each set of bending magnets. The final emittance and momentum spread of the beam will be controlled by wedge foils after the septum magnet which deflects the beam parallel to the equilibrium orbit.

E. Extraction From the Booster

Preliminary considerations indicate that the beam will come out of Period 4 of the booster. The beam will leave the booster through the ceiling in such a manner so as not to conflict with the reverse injection line to the main ring. The antiprotons will be extracted from long straight 4 in the booster. The beam will first be kicked horizontally by 10° to clear the booster elements. Then there will be a vertical dogleg to bring the beam to the cooling ring elevation using two 21° magnets. Two more horizontal bends are then used to direct the beam to the injection point where a 17° horizontal septum is used to bring the beam parallel to the ring. At the present time 12 quadrupoles are envisioned to control the properties of this beam.

G. Injection and Accumulation in Cooling Ring

Cooling and accumulation of many pulses of protons in a major goal of this phase of the cooling ring program. The accumulation scheme must be compatible with the 15-Hertz rate of the Booster. At the same time, it should avoid difficult mechanical devices such as moving septa or magnets, and employ equipment which is within the present state of technology. Accordingly, the scheme proposed is based on electron cooling rf stacking, and single-turn injection.

Conceptually, the momentum aperture is split into two regions, centered at P_1 and P_2, respectively. Each region will accept the full emittance, full momentum spread uncooled beam. Injection is accomplished at momentum P_1. The uncooled beam is rf captured and moved to the neighborhood of momentum P_2, the cooling momentum, where it is stored and cooled.

Injection is accomplished by a kicker located 90° in radial betatron phase downstream of the septum magnet. The septum magnet bends the beam parallel to the equilibrium orbit in the center of the short straight section where X_p is maximum and β_x is small. The kicker again deflects the beam parallel to the equilibrium orbit corresponding to P_1. The position of the septum and the entering beam are chosen to accommodate the emittance and momentum width of the beam, plus the thickness of the septum. This determines the strength of the kicker necessary to deflect

the beam parallel to the equilibrium orbit. The kicker is shut off after one revolution time. Since the effect of a single kicker on the stacked beam would be to induce a large betatron oscillation and cause loss of the stacked beam, a second kicker is placed 90° in betatron phase upstream of the septum magnet. The net effect on the stacked beam is only to cause it to follow a different path during the time new beam is being injected. Errors in betatron phases, beta functions, kicker strengths and kicker timing away from ideal values will cause a small betatron oscillation to be induced in the stacked beam. Experience with cooling has shown that in this condition, i.e., small momentum spread, the cooling of betatron oscillations is fast. The strength required for each kicker is .011 Tm. A kicker with aperture 2" x 6" x 16" will have an inductance of about 2 μH. If driven by a 50Ω line, the rise time will be about 80 nsec, or 10% of the circumference. The charging voltage will be 50 kV.

Accumulation will be accomplished by rf capturing the beam, accelerating the beam to the cooling momentum and stacking it there, as indicated pictorially in the figure. This method allows some margin in the strength of the drag force or cooling rate as compared to the anticipated 15 Hz accumulation rate. The harmonic number of the rf system is 6, (f = 7.5 MHz) corresponding to the number of bunches desired when the cooled beam is recaptured. The voltage required to capture the ±.15% momentum spread is 12 kV. The beam can be moved (2% in momentum) to the stacking region in 2 msec with 3 kV accelerating voltage. The phase oscillation frequency is 6 kHz; thus capture and stacking can be accommodated in several milliseconds with a 15-20 kV rf system with a 1.2% frequency range.

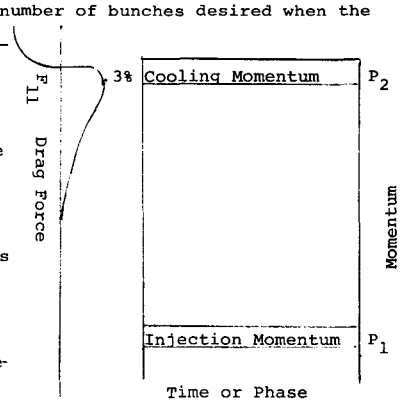

An alternative method, which can also be tested, is to stack in betatron phase space as in electron storage rings. This suffers from several disadvantages. First, there is no margin in the cooling rate since the beam must be damped before the next beam is injected. Second, the cooling is slow for large amplitudes ($V_{\perp p} > V_{\perp e}$) and betatron stacking which is efficient for capturing particles has poor phase space efficiency, leading to large betatron amplitudes, large $V_{\perp p}$, and slow cooling. Third, the large amplitude particles will be outside the electron beam when they have their maximum amplitudes, hence small $P_{\perp}$ (or $V_{\perp p}$), so the cooling rate is further reduced.

VIII. RF System

The rf requirements for the cooling ring are established by the energy and momentum spread of the incident beam together with the required harmonic number and the stacking acceleration rate. These requirements are described in detail at the end of Section VII. The 12 kV mentioned in Sec VII is just the minimum voltage necessary to create bucket area equal to the injected longitudinal emittance. Additional bucket area requirement and the requirement of some accelerating voltage indicate that the rf voltage must be 15 to 25 kV. The rf rest frequency will be near 7.52 MHz and frequency tuning of a few percent about this frequency is necessary. In addition the accelerating resonator vacuum chamber must be of quality consistent with the high vacuum requirements of the cooling ring.

The voltage, frequency, and vacuum requirements can be met nicely with a slightly modified accelerating resonator from the Princeton-Pennsylvania Accelerator (PPA). A cut-away drawing of such a cavity is shown in Fig. 29 . The structure has two accelerating gaps and it is heavily ferrite loaded. The operating frequency of 7.5 MHz can be reached with a ferrite bias current of less than 1000 A at a few volts, so the bias supply requirements are not difficult.

The PPA cavity is driven by two 10 kW rf tetrodes which are mounted directly on the cavity. Anode power for the power amplifier will be delivered by a 14 kV supply which was previously used at PPA as a power supply for the rf test station. Because the cavity has two gaps, each capable of generating a gradient which is almost two times the anode voltage, the system can easily meet the rf voltage requirements. At 200 MeV, protons drifting between gaps move about 13 degrees in rf phase. This phase shift causes about 2 percent decrease in accelerating voltage.

The center drift tube of the cavity consists of stainless steel tubing brazed to cylindrical ceramic insulators. Because the ferrite biasing current flows longitudinally through the cavity shell it is necessary to isolate the accelerating structure from the remainder of the

cooling ring vacuum chamber to prevent a fraction of the biasing current from flowing away from the cavity and into various ground loops paths. Therefore at least one, and probably two, insulators in addition to the accelerating gap insulators will be required. Fortunately, it is very easy to remove the drift tube from the structure and work on it independantly. A four gap drift tube will be fitted with heating devices and installed in the structure making is possible to bake the beam tube in place up to temperatures limited by the ceramic brazing temperature. Because the rf field at the longitudinal mid-plane of the cavity is zero, it is possible to heat the mid-section of the vacuum chamber with heating leads entering at the mid-plane. This connection point is labeled "RF Connection-Resonator to Drift Tube" on Fig. 29.

The rf tetrodes require a few GPM of low conductivity cooling water. The cavity ferrite is cooled by surface contact with 100 ℓ/min of oil which in in turn water cooled in an oil cooling system which must be located near the rf station.

Low level rf signals are to be provided by a very stable voltage controlled oscillator. The frequency can be modulated slightly as required for stacking by a computer controllable function generator. Both beam position and beam phase information will be derived from beam pickups located near the rf station and this information can be fed back to the rf frequency (or phase) generator if necessary. It will be possible to lock the frequency/phase of the rf system to an integral fraction of the booster injection rf frequency/phase for bunch-to-bucket transfer of cooled beam to the booster.

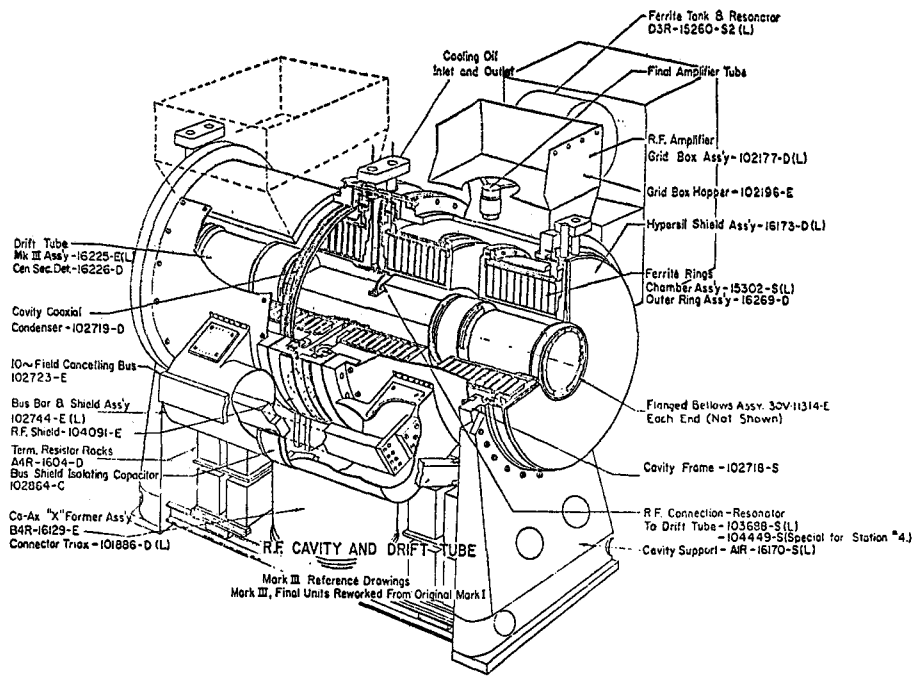

Fig. 29 The Cooling Ring RF Cavity

IX. Radiation Safety

A. Intensity Limiting Collimator

There are several problems associated with the collimator. First, we are not dumping in the momentum dump and hence we lose part of the normal shielding. During tuneup, levels of 3 mrem/hour will be present on top of the dirt berm and during accumulation 90 mrem/hour will be present. The calculation of these predictions has been checked by doing a similar calculation for the normal operation of the momentum dump at 15 Hertz. Before the accumulation experiment is tried, more soil should be placed over the dump area. The neutrons coming up the pipe would be a severe problem, i.e., the levels would be 7.5 rem/hour during accumulation; but, the problem will be controlled by filling the tube with water. The normal intensities will be such that the soil activation and the activation of the cooling water will be no problem. Finally, we must deal with the problem of the activation of the collimator itself. It is expected during tuneup conditions that the collimator will be 0.03R/hour at 1 meter and 2.2 R/hour at contact. The collimator assembly has been designed for easy removal from the pipe. There will be a problem in changing inserts in the collimator, but at these levels, the problem is manageable. The dose estimates mentioned above are for the intensities associated with normal H^- operation. Proton operation or chopper failure will lead to higher dose levels and hence a radiation-activated interlock will be necessary near the second intensity-limiting collimator.

B. Radiation Safety for the Cooling Ring

The dimensions of a beam dump assembly for dumping the protons in the ring have been determined. The system will involve a metal scraper inside the vacuum system, with concrete surrounding this scraper. In the forward direction, one of the bending magnets will be part of the dump. The normal mode for dumping beam will be to use this dump.

One serious problem is the case of a total loss of a stored beam of 10^{11} somewhere around the ring. A scheme of preshielding has been considered for the whole ring. The purpose of the preshielding is to ensure

that no beam of protons leaves the enclosure, i.e., wherever the transverse shielding of the ring elements is too short to stop the protons (mainly the beam pipe between elements), a material (wood, for example) is added to stop the protons when they leave the beam pipe. Also, by dumping the protons close to the ring, one ensures that there is always an appreciable distance for the produced neutrons to spread out before they reach the enclosure wall.

Radiation dose-rate measurements have been made while PRAD was running at a distance of 6 ft from a Pb beam stop. The beam was quite broad compared with our case, but 6 ft is sufficient to allow some averaging to take place (the angular distributions are relatively broad). The beam stop was constructed of Pb bricks and there was some leakage of protons through the cracks in the stop. Even though the beam was a broad beam, there is still an overestimate of the straight-ahead dose. Using the results of this survey, one obtains a dose of 34 mrem at a distance of 16 ft from loss of 10^{11} protons.

There will probably be losses to 5 to 10% on injection in the first section after injection. This section is the section that is closest to the road; hence, this area may require more shielding than just the pre-shielding. Using the same experimental numbers that we had for the previous case, one obtains a dose rate of 0.6 mrem/hour for 10% losses (at a distance of 16 ft from a single loss point at 10^7/sec). Since this dose rate could easily go to 180 mrem/hour (full loss, accumulation conditions), we see that additional shielding would be necessary in this area.

The case that we have not considered here is normal losses around the ring during tuneup or accumulation. Possibly the way to solve this problem is to see how the ring works (with strict administrative control at first), and then add fences or dirt (concrete) shielding as necessary.

X. Instrumentation

Detectors and diagnostics must be provided to measure the performance of the cooling ring and to make dynamic measurements of the electron cooling process. Since the system must work for the small number of antiprotons expected ($\sim 10^6$) per booster pulse during accumulation, strong emphasis is placed on detection systems which can operate for low intensities. At the same time, provision must be made for more routine matters, such as straightening the closed orbit.

The expected dipole field errors and quadrupole position errors are such as to expect a closed-orbit error of the order of one centimeter. Thus, we can expect to find a closed orbit within the aperture with high probability, and can expect to coast a small emittance beam without much difficulty. Detection of coasting beam can be simply accomplished by instrumenting the beam dump with scintillation detectors. Tuning the injection line and injection conditions can be performed using the beam dump signal as a monitor.

Split-cylinder position electrodes, 6 in. in length will be located at every quadrupole. Vertical position will be measured at quads where β_V is maximum, and horizontal position will be measured where β_H is maximum. This provides about three measurements per wavelength for the vertical and four measurements per wavelength for the horizontal. This measurement system is well adapted to a scheme of closed orbit correction which involves only movement of quadrupoles. From each electrode, the spectral density of the signal at a hrrmonic of the revolution frequency, or the autocorrelation function of the signal for a time delay of one revolution period, will be averaged for periods of order one second to obtain the position information. Alternately, the electrodes can be used in a more conventional sum and difference mode, but at somewhat higher intensity ($\sim 10^9$).

Wideband position and longitudinal detectors will be installed to investigate the properties of the cooled beam.

Beam profile will be monitored by a magnesium curtain monitor similar to the sodium curtain employed on the ISR. Since the cooling time is expected to be compatible with the 15 Hz rate of the booster, it would appear that the resolving time of the profile monitor should be no greater than 5 to 10 msec. The electron signal from the monitor is strong enough for this application but is is not yet clear what form the data acquisition should take. Conventional television is too slow for this purpose. The most likely candidate is to use a multichannel plate to amplify the electrons, to accelerate the electrons to a phosphor plate, and to digitize the image on a CCD system.

Other properties of the cooled beam can be inferred by other, by now more conventional systems. Schottky scan can be used for the transverse beam measurements, but probably not for longitudinal measurements. A fast kicker can be used to put a hole in the beam to measure the momentum spread by measuring debunching time. The same kicker can be used with a target-scintillator to infer the betatron amplitude distribution, although one would prefer a less destructive method of measurement. This kicker can be the same one which later extracts the six beam bunches individually. Finally, the neutral hydrogen beam will be present with protons to establish beam size in the cooling region.

XI. Cooling Ring Control System

The control system for the cooling ring will be modeled after the booster accelerator "Serial Camac" control system. The booster system consists mainly of a Xerox 530 computer. Lockheed MAC-16 mini-computers, control consoles, and Camac crates or other types of interfaces (Fig. 30). For the cooling ring, one console, one mini-computer, approximately five serial Camac crates, and associated control system hardware will be added to the beam line control system (Fig. 31).

Using this type of system has several distinct advantages. Existing equipment and designs may be used which will minimize costs due to engineering, software, system debugging, and spare parts inventory. Operation of the cooling ring may be accomplished from either the cooling ring control room or later the accelerator main control room. This system will also be easily expandable for future needs as the cooling ring is developed.

The control room will be located in the west booster gallery fan room. This area has ample room for the console and other monitoring equipment. It has heating and air-conditioning and will provide a good environment for both humans and equipment. This room also allows easy access to the cooling ring, the linac and booster galleries, and other creature comforts.

Serial Camac crates will be distributed in the control room, injection, and cooling straight areas of the ring near the equipment they control. The mini-computer will be located in the accelerator MAC room where most of the other mini-computers are located.

Some additional features the control system provides are computer-generated plots, equipment-status monitoring, file storage of machine operating conditions, and closed loop control of critical machine parameters.

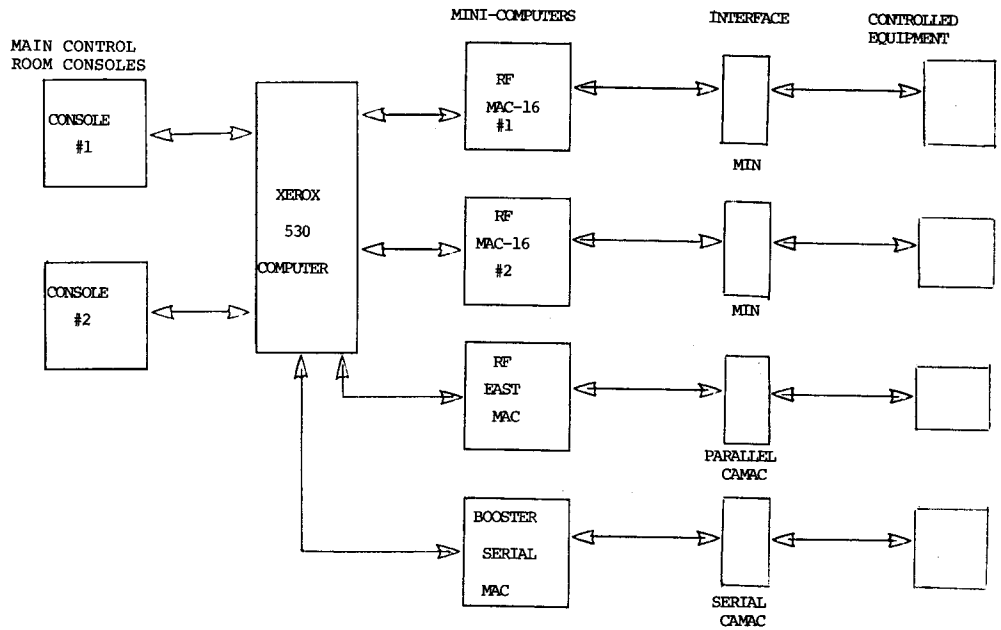

Fig. 30 Booster Control System

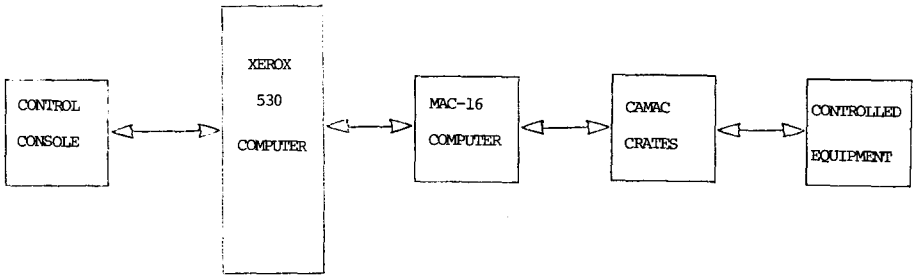

Fig. 31 Cooling Ring Control System

APPENDIX I

FERMILAB $\bar{p} \times p$

$\sqrt{S} = 500/2000$ GeV

GOALS: Proton "cooling" experiment

1. Electron "cool" 200 MeV protons (10^7) 10/78
2. Accumulate 200 MeV protons (10^{10}) 12/78
   $\bar{p}$ experiment
3. First $\bar{p}$ into cooling ring 1/79
4. First $\bar{p}$ into main ring 3/79

STEP I. PRODUCE $\bar{p}$, DECELERATE $\bar{p}$ COOL $\bar{p}$ (6 SEC.)

1. Accelerate 200 MeV H^- in Linac and inject into booster (normal operation).
2. Strip H^- at injection into booster to load booster with p (normal operation).
3. Inject 8 GeV p into main ring and accelerate to 100 GeV (normal operation).
4. Extract 100 GeV p into target and produce 5.2 GeV $\bar{p}$.
5. Inject 5.2 GeV $\bar{p}$ into booster and decelerate to 200 MeV.
6. Inject 200 MeV $\bar{p}$ into cooling ring and "cool" with 110 KeV e^-.

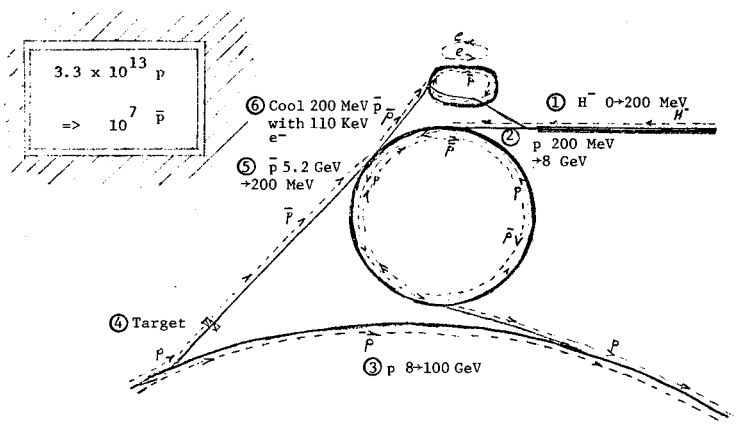

STEP II. ACCUMULATE $\bar{p}$ (3 HOURS)

1. Step I above. Take 1/46 $\left(= \frac{\text{radius cooling ring}}{\text{radius main ring}}\right)$ of main ring beam and produce one full turn of $\bar{p}$ for cooling ring.
2. In one booster cycle (66 ms) cool $\bar{p}$ (56 ms) and momentum stack (10 ms to move 10 MeV/c) with rf into stacked $\bar{p}$ beam.
3. Repeat 1 and 2 above 46 times (3 seconds) to achieve an additional 10^7 $\bar{p}$ in stack (this unloads all p from main ring).
4. Use the electron beam at a slightly different momentum (~10 MeV/c) to keep stacked $\bar{p}$ "cold" while main ring is being loaded with p (3 sec).
5. Repeat 3 and 4 above 1800 times (3 hours) to accumulate $>10^{10}$ $\bar{p}$ in cooling ring.

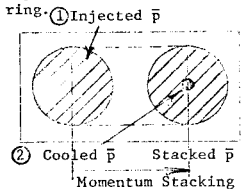

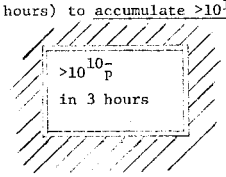

Cooling Ring Magnetic Aperture Schematic of Beams

STEP III. LOAD MAIN RING WITH $\bar{p}$ (~15 MIN)

1. Bunch $\bar{p}$ with 8.25 MHz rf into 6 bunches which will match into every 4th bucket in booster (33 MHz).
2. Simultaneously inject H^- into booster to tune booster for $\bar{p}$. H^- survives ~100 turns because of booster vacuum.
3. "Ping" out ~10^8 $\bar{p}$ into booster, accelerate to 8 GeV and inject into main ring. Repeat until all machines tuned for $\bar{p}$.
4. Extract $\bar{p}$ from cooling ring into booster, accelerate to 8 GeV and inject into main ring.
5. Accelerate $\bar{p}$ in main ring to 250 GeV and hold ($\bar{p}$ need to be stored at high energy to avoid beam blow-up due to scattering on residual gas in the vacuum chamber).

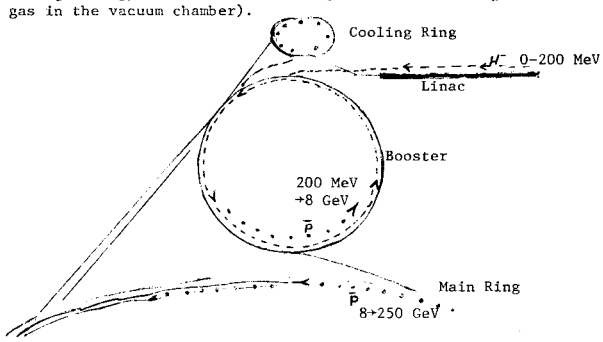

STEP IV. LOAD MAIN RING WITH p (~15 MIN)

1. Load cooling ring with p (10^{12}), cool and bunch into 6 rf bunches.
2. Decelerate $\bar{p}$ in main ring to 8 GeV.
3. Inject p into booster, accelerate to 8 GeV and inject into main ring such that p and $\bar{p}$ will intersect at D0 and B0.
4. Accelerate p (10^{12}) and $\bar{p}$ (10^{10}) simultaneously to 250 GeV.

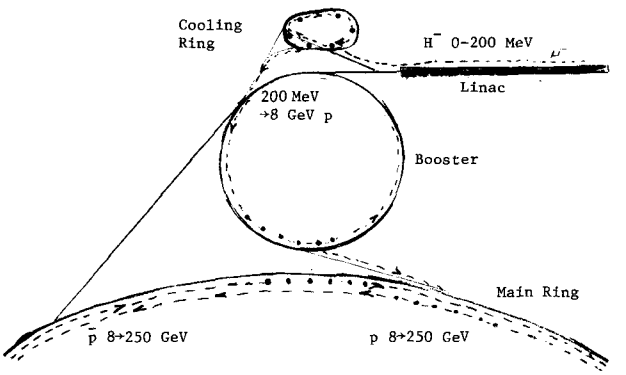

STEP V. COLLIDE 250 GeV p x 250 GeV $\bar{p}$

1. Turn on "low beta" at E0 and B0. $\sigma_{beam} \approx .15$ mm.
2. Luminosity L >2 x 10^{28} cm^{-2} sec^{-1} yield >1000 interactions/second at each interaction region.
3. Beam lifetime ~3.5 hours.
4. In Energy Doubler L >10^{30} $cm^{-2}sec^{-1}$ for 1000 GeV p x 1000 GeV $\bar{p}$.

Appendix II

Mg Jet Monitor

A magnesium ribbon jet will be installed in one short straight section Fig. 1. The momentum dispersion here allows a useful profile of the beam (as contrasted to the long straights). The device will be mounted in a 12", 6 port cross such that the jet shoots horizontally across the beam and at a 45° angle (allows 2^{d} profile with one jet) to it. The actual ribbon generator (oven plus slit assembly) is being made for us by the Instrumentation Systems Center, University of Wisconsin.

The third orthogonal axis of the cross will contain the electron collection and detection elements as depicted in Fig. 2. The novel feature of this detector is the RA (resistive anode) readout. Based on the charge division location of the centroid of individual multiplied events, such films on substrates with contacts and associated electronics are available commercially. Rates of several hundred thousand/s can be tolerated (which we will see is more than adequate for our lowest anticipated beam currents and which we can easily avoid exceeding by lowering the Mg oven temperature for use with higher currents). Such a detector is essentially noiseless since the channel plates have dark currents <1/s.

As an example of low beam current operation consider a Mg oven temperature of $750^{o}K$ (P=0.03 torr). For our slit geometry and for (anti)protons of $\beta \sim 0.5$ we calculate

$$R_{e^-} = 5 \times 10^{6}/s$$

which is based on 10^{7} (anti) protons circulating and a Mg density of $2 \times 10^{10}/cm^{3}$ in a 0.5 mm thick ribbon at intersection. The collection and multiplication of electrons is essentially 100% efficient so that profiles pictures of the beam each 10 msec (the cooling tune scale of interest) will be composed of ~500 "points".

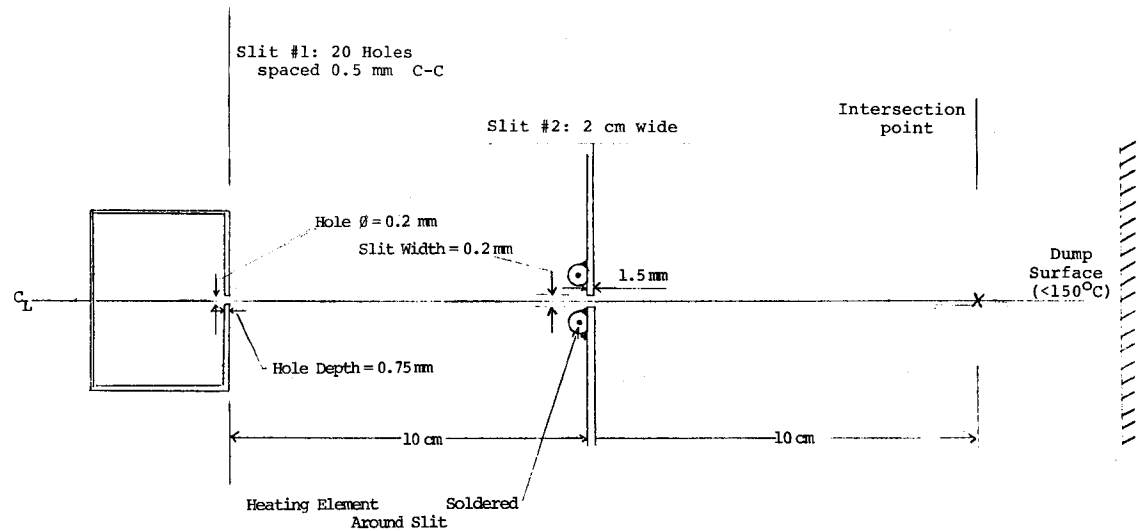

Fig. 1 Magnesium Oven and Jet Geometry

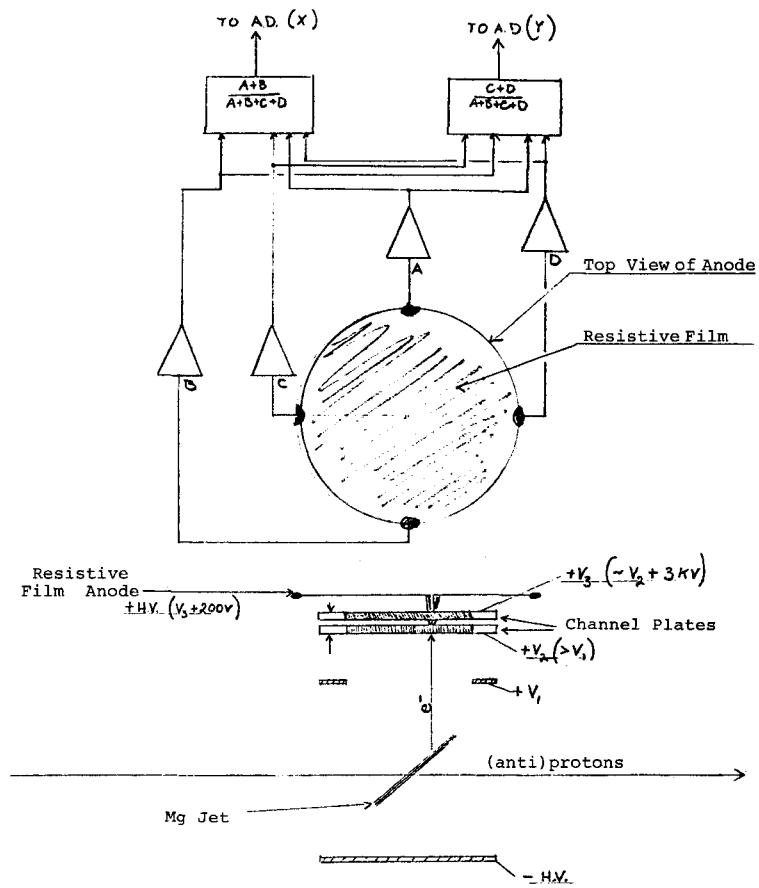

Fig. 2 Magnesium Jet Electron Image Readout System

XII. Bibliography

1. V.L. Auslander et al., Fazovaya Naustoichivost Intensivnogo Electronnogo Puchka v Nako Pitele, Atomnaya Energiya 22, 210 (1967).
2. V.L. Auslander et al., Experimentalniye Danniye po Vzaimodeistviyu Puchkov pre Vstreche, Atomnaya Energiya 22, 213 (1967).
3. G.I. Budker, Effecktivniy Metod Dempfirovania Kolebaniy Chastitz v Protonnix y Antiprotonix Nako Pitelyax, Atomnaya Energiya 22, 346 (1967).
4. R.L. Gluckstern, Intersecting Storage Accelerator Notes; Electron Cooling of Protons in Isabelle, Preprint, CRISP 71-24, Isabelle Project, August 23, 1971.
5. G.I. Budker et al., First Experiments on Electron Cooling, Preprint, Inst. of Nucl. Phys., Novosibirsk, USSR (1974).
6. G.I. Budker et al., Preliminary Experiments on Electron Cooling, IYaF Preprint 74-87, Inst. for Nucl. Phys.. Novosibirsk (1974). (Translated by Brookhaven National Laboratory, BNL-TR-593.)
7. V.V. Anashin et al., Experimental Facility for Electron Cooling, IYaF Preprint 74-86, Inst. for Nucl. Phys., Novosibirsk (1974). (Translated by Brookhaven National Laboratory, BNL-TR-588.)
8. G.I. Budker, et al., Kinetics of Electron Cooling, IYaF Preprint 74-85, Inst. for Nucl. Phys., Novosibirsk (1974). (Translated by Brookhaven National Laboratory, BNL-TR-591.)
9. G.I. Budker et al., New Experimental Results of Electron Cooling, Preprint 76-32, Nucl. Phys. Inst., USSR. Presented to the All Union High-Energy Accelerator Conference, Moscow, October 1976.
10. G.I. Budker et al., Experimental Studies of Electron Cooling, Particle Accelerators, 7, 2044 (1976).
11. C. Rubbia, Confinement of Strong Electron Current for (Anti)-Proton Cooling, EP Internal Report 76-17, CERN, Geneva (1976).
12. G.I. Budker et al., Experimental Study of Electron Cooling, IYaF Preprint 76-33, Inst. for Nucl. Phys., Novosibirsk (1976). (Translated by Brookhaven National Laboratory, BNL-TR-635.)

13. M.N. Rosenbluth, Ion Cooling by Electrons in a Strong Magnetic Field, private communication (June, 1977).

14. Ya.S. Derbenev and A.N. Skrinsky, Effects of an Accompanying Magnetic Field in Electron Cooling, Preprint, Inst. of Nuclear Phys., Novosibirsk, USSR (1977).

15. N.S. Dikanski, et al., The Influence of the Effects of Space Charge on Electron Cooling, Preprint, Inst. of Nucl. Phys., Novosibirsk (1977).

16. Ya.S. Derbenev and A.N. Skrinsky, The Kinetics of Electron Cooling of Beams in Heavy Particle Storage Rings, Particle Accelerators, 8, 1 (1978).

17. C. Rubbia, Relativistic Electron Cooling for High-Luminosity Proton-Antiproton Colliding Beams at Very High Energies, to be published in Proc. from LBL Workshop for Producing High Luminosity-High Energy Proton-Antiproton Collisions, March 27-31, 1978.

18. P. McIntyre and A. Ruggiero, Accommodating Stochastic Cooling at Fermilab, to be published in Proc. from LBL Workshop for Producing High Luminosity-High Energy Proton-Antiproton Collisions, March 27-31, 1978

19. A.G. Ruggiero, High-Energy Electron Cooling, Fermilab Physics Note FN-311/1503, June, 1978.

☆ U.S. GOVERNMENT PRINTING OFFICE: 1978—650-128